



# JOURNAL OF **EMERGING INVESTIGATORS**

VOLUME 2, ISSUE 5 | MAY 2019  
[emerginginvestigators.org](http://emerginginvestigators.org)

## **Music to the ear** Investigating dissonance and timbre

### **Combatting insulin resistance**

A potential early intervention-based diabetes treatment

### **3D-printed tissue scaffolds**

Cost-effective tools for regenerating bone tissue

### **Potato plastics**

Making bioplastics from sweet potato peels

### **Myocarditis treatment effects**

Looking into cell density and proliferation after treatment



# JOURNAL OF EMERGING INVESTIGATORS

The Journal of Emerging Investigators is an open-access journal that publishes original research in the biological and physical sciences that is written by middle and high school students. JEI provides students, under the guidance of a teacher or advisor, the opportunity to submit and gain feedback on original research and to publish their findings in a peer-reviewed scientific journal. Because grade-school students often lack access to formal research institutions, we expect that the work submitted by students may come from classroom-based projects, science fair projects, or other forms of mentor-supervised research.

JEI is a non-profit group run and operated by graduate students, postdoctoral fellows, and professors across the United States.

## EXECUTIVE STAFF

Mark Springel **EXECUTIVE DIRECTOR**  
Haneui Bae **COO**  
Qiyu Zhang **TREASURER**  
Michael Mazzola **DIRECTOR OF OUTREACH**

## BOARD OF DIRECTORS

Sarah Fankhauser, PhD  
Katie Maher, PhD  
Tom Mueller  
Lincoln Pasquina, PhD  
Seth Staples

## EDITORIAL TEAM

Jamilla Akhund-Zade **EDITOR-IN-CHIEF**  
Olivia Ho-Shing **EDITOR-IN-CHIEF**  
Michael Marquis **EDITOR-IN-CHIEF**  
Brandon Sit **MANAGING EDITOR**  
Laura Doherty **MANAGING EDITOR**  
Michelle Frank **HEAD COPY EDITOR**  
Sonia Kim **HEAD COPY EDITOR**  
Naomi Atkin **HEAD COPY EDITOR**  
Alexandra Was, PhD **PROOFING MANAGER**  
Erika J. Davidoff **PUBLICATION MANAGER**

## SENIOR EDITORS

Kiana Mohajeri      Chris Schwake  
Laura Doherty      Kathryn Lee

**FOUNDING  
SPONSORS**



# Contents

VOLUME 2, ISSUE 5 | MAY 2019

- A Taste of Sweetness in Bioplastics** 4  
Jennifer Tsai, Yvonne Fu, Karen Ho, and Dino Ponnampalam  
Kang Chiao International School, New Taipei City, Taiwan
- Combating Insulin Resistance Using Medicinal Plants as a Supplementary Therapy to Metformin in 3T3-L1 Adipocytes: Improving Early Intervention-Based Diabetes Treatment** 9  
Dia Jayram and Leya Joykutty  
American Heritage School, Plantation, Florida
- Examining What Causes Perceived Dissonance in Musical Intervals and the Effect of Timbre on Dissonance** 15  
Michelle Hsu and Hui-Yin Hsu  
Locust Valley High School, Locust Valley, New York
- 3D Printed Polymer Scaffolds for Bone Tissue Regeneration** 22  
Nipun U. Jayatissa and Sarit Bhaduri  
Maumee Valley Country Day School, Toledo, Ohio
- Cytokine Treatment for Myocarditis May Directly Impact Cardiomyocytes Negatively** 28  
Jacob Kasner and Leya Joykutty  
American Heritage School, Plantation, Florida

All articles are copyright © 2019 to their respective authors. All JEI articles are distributed under the attribution non-commercial, no derivative license (<http://creativecommons.org/licenses/by-nc-nd/3.0/>). This means that anyone is free to share, copy and distribute an unaltered article for non-commercial purposes provided the original author and source is credited.

# A Taste of Sweetness in Bioplastics

Jennifer Tsai, Yvonne Fu, Karen Ho, and Dino Ponnampalam

Kang Chiao International School, New Taipei City, Taiwan

## SUMMARY

In this study, we used an agricultural waste commonly found in Taiwan, sweet potato peels, to make bioplastic. We manipulated the amount of glycerol added when making the plastic and measured the resulting plastic's properties. We predicted that reducing the amount of glycerol would result in a firmer and less malleable plastic because glycerol acts as a plasticizer, preventing the polymers from forming brittle, inflexible structures. The process began with extracting starch from sweet potato peels. We also ran the peels and their starch under a flame test to investigate the type of metal ions they contained, which we determined to be  $\text{Cu}^{2+}$  and  $\text{Cu}^+$ , respectively. Then, we made bioplastic by heating up the starch mixture with acetic acid, different amounts of glycerol, and water. Allowing the mixture to set, we were left with a thin piece of plastic film. In the final stage of the experiment, we conducted a stress test to evaluate the malleability of plastic mixtures. Our results supported our initial prediction as the plastic containing the greatest amount of glycerol expanded the most, indicating that it had the greatest malleability. We concluded that the ratio of 1:2.4 starch to glycerol would yield the ideal plastic film with a flexible yet firm texture, properties which allow for the plastics to be molded into different structures yet still retain their shapes. Even though we didn't manage to make a substantial amount of plastic, we have determined a recipe for making bioplastics from agricultural waste such as sweet potato peels. This opens a door for possibilities in slowing down the rate of pollution caused by widespread use of conventional plastics.

## INTRODUCTION

Plastic, a word that originally meant "pliable and easily shaped", is a fundamental material found in all parts of human society [1]. In 1907, Leo Baekeland invented Bakelite, the first fully synthetic plastic [1]. The issue of synthetic plastic gained public attention after World War II, when plastic debris was observed in the ocean [1]. During the 1970s and the 1980s, people were even more concerned about plastic waste, as they became aware of the longevity of plastic [1]. Today, plastic is found everywhere in our lives — from plastic bottle caps to straws, bags, and milk jugs. This purported miracle material has been a building block for development, but now we're surrounded by it because it cannot be decomposed in a short period of time [2]. Furthermore, more than 40% of

plastics are used only once, which is a serious environmental issue [2]. Therefore, we wondered if there was a way for us to alter the nature of plastic to make it biodegradable in nature.

To achieve this goal, we used sweet potato peels, an agricultural waste commonly found in Taiwan, to make bioplastic. Sweet potatoes are one of the most common starches in Taiwan; they are added in porridges, fried in the shapes of spheres in food stalls in night markets, and even sold as baked sweet potatoes in convenience stores. Most of the time, however, the peels are forgotten and thrown straight into the trash bin. We believe that using sweet potato peels to make plastic has the potential to alleviate the carbon footprint petroleum-based plastic has on the environment. Starch is an ideal choice for bioplastic because it has high elongation, tensile, and flexural strength, meaning after processing, starch-based plastic can be molded into different forms for various purposes [3]. Not only were we recycling kitchen waste to produce useful materials, but we were also giving these peels more purpose, fully utilizing sweet potatoes from porridges to the peels in plastics. Therefore, we wanted to test whether it was possible to make plastic from the peels, to turn waste into a usable product which may alleviate some of the environmental issues we are facing today.

In this study, we adopted the measurements provided by the Royal Society of Chemistry but also modified the measurements to form the firm-yet-flexible films we wanted [4]. We manipulated the amount of glycerol added to the starch and acetic acid to observe the differences in physical properties of the plastic films. We wanted to make plastics with different malleability to find out which sample had the highest strength and flexibility; such plastics can be potentially shaped into different structures but still hold their shape. The biologically based plastics we made from starch can be categorized as biodegradable plastics because the materials used to make the plastic, including starch, acetic acid, and glycerol, are all biodegradable. On the other hand, conventional plastics take around 400 years to biodegrade [2]. We hypothesized that adding less glycerol would cause the plastic to be firmer and more inflexible. This is because glycerol prevents polymers from having brittle, inflexible textures. The purpose of our experiment was to find the ratio between starch and glycerol that yielded the most firm-yet-flexible plastic.

## RESULTS

There were four components to our experiment in our quest to make bioplastic: flame tests, extraction of starch from sweet potato peels, making sweet potato peel plastic,

and stress tests. First, we used a flame test to determine the presence of metal ions in the sweet potato peels. Knowing the ions found in the sample of sweet potatoes assisted in our plastic construction because then we could manipulate the properties of these ions. Different colors indicated the presence of different ions (**Table 1**). We placed some ground peels onto the wire and positioned the wire over the flames. The color of the flames turned bluish-green for sweet potato peels, indicating the possible presence of copper ions,  $\text{Cu}^{2+}$ , in the peels (**Table 1**) [5]. When we conducted a flame test on the starch and the plastic samples containing 5 mL and 8 mL of glycerol, the color of the flame had a tint of green, indicating changes to the copper ions. The color green suggested the presence of  $\text{Cu}^+$  metal ions (**Table 1**). However, when we conducted the flame test for 22 mL and 27 mL glycerol plastic, there was no color change (**Table 1**). This signified that the  $\text{Cu}^+$  ion that was present in the 5 mL and 8 mL glycerol plastic flame test was no longer present. A possible reason could be the excessive amount of glycerol used in the 22 mL and 27 mL glycerol plastic.

In the second part of the experiment, extracting the starch, we were able to obtain 18.35 g of starch in total. We then decided to compare how different amounts of glycerol would affect the quality of the plastic. Thus, we created two batches of plastic mixture: both had the same amounts of water, starch, and acetic acid with different quantities of glycerol, 22 mL and 27 mL; the 22 mL sample had a ratio of 1:2.4 starch to glycerol and the 27 mL sample had a ratio of 1:2.9.






After heating the solutions over a hot plate for 40 minutes, we noticed a change of texture. The solution was no longer liquid-like; instead, the solution was slimy and sticky. However, when we measured the pH of the plastic, the solution was very

acidic, yielding a pH of 3.5. Not only was the solution acidic, but the steam from boiling the solution was also very acidic, with a pH of 4. Thus, we added ammonia water, which is a weak base, to neutralize the solution. After adding ammonia water to the solution, the solution gradually turned from a pH of 3.5 to 7. Then we poured out the solution from the beakers into separate petri dishes.

We allowed the mixtures to set for three days. As the mixtures still retained a gel-like texture, we heated the mixtures for another 20 minutes to burn off the excess liquid, then allowed them to cool down again. However, the sample containing 27 mL of glycerol did not form a sturdy plastic film. Thus, we decided to put one of the 27 mL glycerol samples into the freezer and observe it for property changes. After placing the sample in the freezer for a day, the plastic remained gel-like (**Figure 1**).

Based on these results, we concluded that large amounts of glycerol (27 mL) affected the plastic mixture so that they could not form into a firm texture. Thus, we decided to create two other samples of plastic, each with significantly lower amounts of glycerol, one with a ratio of 1:1.3 starch to glycerol and the other with a ratio of 1:0.7 starch to glycerol. We heated the mixture containing starch, water, acetic acid, and glycerol for 20 minutes then left it to set for a day. However, the starch we used this time was not in powder form; instead, the starch was in clumps. In addition, the starch we used this time was from sweet potato peels which had already been used for starch extraction. Therefore, the starch yield might have been lower compared to the first time we extracted starch from the peels.

After the plastic mixtures settled into thin films, we conducted a malleability test by dropping a volleyball onto 5 mL, 8 mL, 22 mL, and 27 mL glycerol plastic for five times. After dropping the volleyball five times, we observed and measured the increase in area of the plastic sample. The 22 mL glycerol sample expanded the most, as its area increased by 337% and the difference in area before and after the malleability test was the greatest (**Table 2, Figure 2**). In contrast, the 27 mL glycerol sample expanded the least, as its area only increased by 3.45% and the difference in area before and after the malleability test was the least.

Original Flame Color	Sweet Potato Peel Flame Color	Sweet Potato Peel Starch Flame Color	Sweet Potato Peel Plastic (5 mL glycerol plastic) Flame Color	Sweet Potato Peel Plastic (22 mL glycerol plastic) Flame Color
Orange	Bluish-green	A tint of green	A tint of green	Orange
				
None	$\text{Cu}^{2+}$	$\text{Cu}^+$	$\text{Cu}^+$	None

**Table 1. Flame Test from Different Plastic Samples.** The comparison of different flame colors emitted from different samples of plastic and sweet potato peel used indicate the presence of ions in the sample. The original flame color serves as a basis for observing the color change in the flame tests. The ion detected in the samples were mainly copper ions, as seen through the picture of sweet potato peel, sweet potato peel starch, and 5 mL glycerol plastic. The flame test for plastic samples that contain 22 mL glycerol shows no color change in the flame test. This indicates that the  $\text{Cu}^+$  ion is no longer detectable. A possible explanation for the absence of  $\text{Cu}^+$  ions may be due to the excessive amount of glycerol present.

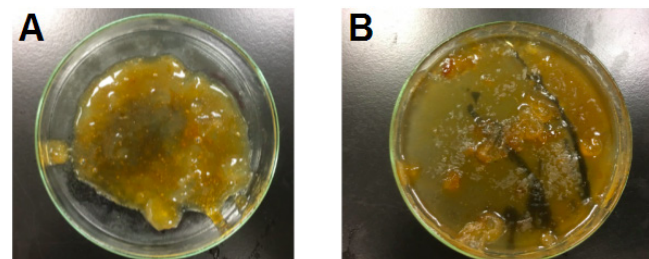


**Figure 1. 27 mL glycerol plastic sample and 22 mL glycerol plastic sample.** A) The 27 mL glycerol plastic sample after being in the freezer for one day. B) The 22 mL glycerol plastic sample after being in the freezer for one day. The plastic has already settled into a thin film, allowing the stress test to be conducted.

In addition to the malleability test, we tested whether our plastic dissolves in water or not. After soaking a 1.0 g sample of the 22 mL glycerol plastic in water with a magnetic stirrer for 30 minutes, the plastic did not dissolve.

**DISCUSSION**

From the flame test results (Table 1), we noticed that although there were tints of green for 5 mL and 8 mL plastic (1:0.54 and 1:0.87 starch to glycerol ratio), the flames returned to their original orange color for 22 mL and 27 mL samples (1:2.4 and 1:2.9). We speculated that copper was no longer observed for 1:2.4 and 1:2.9 starch to glycerol samples because the quantity of glycerol was too great to the extent that the metal ions in the starch were no longer detectable. Moreover, although we speculated that the bluish-green colored flames might be indicators of the presence of Cu<sup>2+</sup> ions, other metal ions such as zinc and phosphorus also emit bluish-green flames [6]. We couldn't be certain that the bluish-green flames observed derived solely from copper ions. One area of improvement to consider, therefore, is to conduct more trials on the starch and each plastic sample to increase data accuracy.

Based on our experimental results, we concluded that the plastic with a starch to glycerol ratio of 1:2.4 (the one with 22 mL of glycerol) yields a firm yet flexible plastic film. We demonstrated this by making different samples of plastic with 91.75 mL water, 9.175 g starch, 3.67 mL acetic acid and different volumes of glycerol (5mL, 8mL, 22 mL, and 27mL) to compare their properties. The amount of glycerol affected the properties of the plastic. We could tell the difference just from raw observation: the 27mL and 22 mL glycerol plastic was more gel-like compared to the 8 mL and 5 mL glycerol plastic. This suggested that as the amount of glycerol increases,

the tensile strength of the plastic will decrease. The 27 mL glycerol plastic's area increased by 3.45% and the 22 mL glycerol plastic's area increased by 337%. This alluded to the fact that as the amount of glycerol increases, the malleability of the plastic also increases (Table 2, Figure 2).

Recalling the results from the solubility test, the plastic we made has a wide range of uses, as the plastic remained intact when soaked in water. This feature allowed the plastic to contain a variety of matter, including liquids. Also, the plastics we made consist mainly of natural ingredients, such as sweet potato peels. The synthetic ingredients added during the process of making plastic are also non-toxic ingredients, such as glycerol and acetic acid. Therefore, we predicted that our plastic is biodegradable, as the ingredients added do not harm the environment and are easy to decompose. Given these properties, our plastic was eco-friendly and had a wide range of usages. For the 22 mL glycerol plastic, the plastic did not dissolve in water and the area expanded significantly after dropping the volleyball onto the sample five times. This showed that our plastic was very malleable. Hence, the 22 mL glycerol plastic could be made into thin plastic films that can be used as plastic wrappings for food. The other plastic samples where less glycerol was added, such as the 5 mL and 8 mL glycerol plastic, could be used for making sturdier products, such as plastic utensils. However, the cost behind making these bioplastics served as a concern. Taking note that 22 mL of glycerol costs 1 USD and 22 mL of glycerol only yields about 5 grams of plastic, we could infer that the cost of making bioplastics is significantly greater than conventional, petrol-based plastic. However, the cost of making bioplastics could possibly be reduced if bioplastics become a mass product.

Numerous factors could have affected our experimental

	27 mL glycerol plastic	22 mL glycerol plastic	8 mL glycerol plastic	5 mL glycerol plastic
Texture	The plastic is mainly in liquid form. Yet we can still find certain areas where a plastic film has formed. [Figure 2]	The plastic is gel-like with clumps of plastic within the solution. [Figure 2]	The plastic has clumps of starch in it and it is mushy.	The plastic has clumps of starch in it and it is mushy.
Malleability Test Conducted in June 2018	The area of the plastic increased by 0.03% (from 3.801cm <sup>2</sup> to 3.932 cm <sup>2</sup> ).	The area did not change.	The sample was not testable.	The sample was not testable.
Malleability Test Conducted in January 2019	The area of the plastic increased by 3.45% (from 3.801 cm <sup>2</sup> to 3.932 cm <sup>2</sup> ).	The area of the plastic increased by 337% (from 3.801 cm <sup>2</sup> to 16.62 cm <sup>2</sup> ).	The area of the plastic increased by 39.7% (from 3.801cm <sup>2</sup> to 5.309 cm <sup>2</sup> ).	The area of the plastic increased by 62.0% (from 3.801cm <sup>2</sup> to 6.158 cm <sup>2</sup> ).

**Table 2. Comparison and Summary of Plastic Samples by Texture.** Results from the malleability test #1 and #2 demonstrate the plastic made from 22 mL of glycerol has the highest percentage increase in area (337%), which fits our criteria of a malleable yet firm plastic.

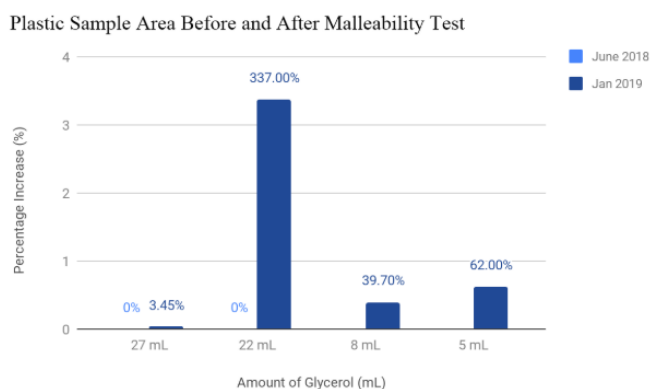


**Figure 2. Percentage Increase of Plastic Samples After Malleability Test.** The percentage increase in the area of different plastic samples indicates the sample's malleability. As seen through the graph, the plastic sample with 22 mL of glycerol expanded the most whereas the 27 mL glycerol plastic increased the least. This suggests that the 22 mL glycerol plastic is very malleable compared to the other three trials. The absence of data for the June 2018 5 mL and 8 mL glycerol plastic experiment is due to the fact that we were unable to conduct the malleability test from the plastic sample we produced at that time.

results. First, for the flame test, contamination from the equipment used could have increased the uncertainties. For instance, if the nichrome wire was not cleaned enough for every trial, there may have been residue of other chemical compounds remaining on the wire, resulting in inaccuracies. Second, when making the plastic films, inconsistencies with the surface area and quality of the starch could also have affected the properties of the plastic. For instance, the plastic samples made from starch in powder form, having greater surface areas, could have expanded more evenly in the stress tests than the samples made from the starch in clumps. Moreover, although we tried to ensure that the surface areas of the plastic samples were consistent for each variation of the stress test, we could not be certain that the amount of plastic experimented on was the same throughout. The more plastic we had, the greater in area the plastic sample would expand. To correct this error, each sample could be weighed to make sure the same amount was used. Although the results showed promise for biodegradable, sweet potato starch-based plastic, more investigations need to be conducted to make sure it could substitute for conventional petroleum-based plastic. Further research should be done to test its properties such as heat resistance and durability.

There were discrepancies between the results recorded in June 2018 and January 2019. We believed they may be due to the following reasons. First, we failed to maintain some factors constant, including the conditions in which we conducted the experiments and the form of the starch. For instance, the total rainfall received in June 2018 in Taipei is 119.8mm, while the precipitation in January 2019 is 45.0mm [7]. The low humidity experienced in January 2019 may have caused the elongation properties to be more prominent than in June 2018 because more water had evaporated out after 40 minutes on the hot plate. Moreover, the forms of the starch experimented on were inconsistent. The starch used for all the trials in January 2019 were all in powder form, yet the starch for 5 mL and 8 mL samples were in clumps rather than powder form.

Given this reason, we believed the results from January 2019 were more accurate since a physical characteristic of starch was kept constant. From the results of the January 2019 stress test, we concluded that a starch-to-glycerol ratio of 1:2.4 yields a malleable-yet-firm structure, thus producing an excellent plastic film. Yet we could not neglect the major discrepancies between the results from June 2018 and January 2019. For instance, the film from June 2018 expanded 0% while the one from January 2019 expanded 337%. We decided to base our discussion around the results from January 2019. Having made careless experimental errors such as not keeping a variable constant throughout all trials (whether the starch is in powder form or in clumps), we believed the results from January 2019 were more reliable. This is also why if we were to perform a third set of trials, we predict the results will be closer to the results from January 2019. The range in data results illustrated how variable

bioplastic is; for instance, with a slight change in humidity, there could be drastic changes to plastic properties.

Creating bioplastics involved careful monitoring of all kinds of variables; thus, bioplastic industries around the world may have the same intention of producing an alternative to petroleum-based plastic, yet depending on variables such as temperature, humidity, source of plastic, time, etc., they could all be creating products with variable properties. By demonstrating the plastic with a starch to glycerol ratio of 1:2.4 (the one with 22 mL of glycerol) yielded a firm yet flexible plastic film, we offered insight into the rapidly expanding world of the bioplastic industry, where people are constantly seeking for alternatives to petroleum-based plastic. With this study, we aimed to show there is a possibility to find a substitute in sweet potatoes.

## METHODS

### Flame Test

Dry sweet potato peels were placed in a mortar and ground with a pestle. Then, 2 mL of methanol was added into the mortar while continuing the grinding process. After the sweet potato peels were ground into a mushy texture, a nichrome wire was used and the tip of the wire was coiled. Nichrome, which consists of 80% nickel and 20% chromium, is an ideal material for the flame tests because it is oxidation resistant and has a melting point of 1400°C [8]. The wire served as a medium to deliver the peels onto the flames. Since the wire was likely to be contaminated, the nichrome wire was cleaned by dipping the tip of the wire into hydrochloric acid and burning it off with a flame. This step was repeated until the tip of the nichrome wire is cleaned and not contaminated. Finally, after placing a sweet potato peel sample at the tip of the nichrome wire and placing it over a flame, color changes were observed and the results were recorded. The results from the flame test could give us insight into the ions present in the particular sweet potato sample used. We believed knowing this information can help us with constructing bioplastics.

### Extracting Starch from Sweet Potato Peels

To extract the starch from the sweet potato peels, we added enough water to submerge and grind the peels. Then the water solution was transferred into another beaker, leaving the potato peels behind in the mortar. Water was then added into the sweet potato peels again and the sweet potato peels were ground until the solution became misty. The water solution was transferred into the beaker and allowed to settle in the beaker for five minutes. When the starch settled at the bottom of the beaker, water was gently poured out of the beaker, leaving the starch behind. Then the starch was removed from the bottom of the beaker and placed on a petri dish to dry.

### Making Sweet Potato Peel Plastic

An experimental protocol written by Royal Society

Chemistry was referred to and the measurements provided were followed (Royal Society of Chemistry). 91.75 mL water, 9.175 g starch, 3.67 mL acetic acid and different volumes of glycerol (propan-1,2,3-triol) (5mL, 8mL, 22 mL, and 27mL) were added into four different beakers. The quantities 22 mL and 27 mL were chosen initially based on the ratio provided by the Royal Society of Chemistry. However, after we discovered the 27 mL plastic was not firm yet flexible, we decreased the amount to 5 mL and 8 mL to see the difference in plastic properties. Then, the mixtures were mixed and placed over a hot plate to heat up the mixture. The mixtures were carefully brought to a light simmer and kept over the flame for around 40 minutes. During the heating process, an indicator paper was used to measure the pH. Enough ammonia water was added to neutralize the water, and the pH value was tested after each addition. After the mixture has been heated for 40 minutes, the mixtures were poured into petri dishes and were allowed to dry and solidify.

### Stress Test

A piece of the plastic sample was cut out and placed onto a clean piece of cardboard. Then, the borders of the plastic sample were outlined with a marker. The approximate area of the plastic was calculated and the value was recorded. From the same height of 84cm, a Molten V5M5000 volleyball that weighed 279.15 g was dropped onto the plastic sample five times and the expanded area of the plastic sample was recorded. The ball was dropped exactly five times to increase the possibilities of it actually hitting the sample and expanding the area of the sample.

**Received:** November 29, 2018

**Accepted:** February 14, 2019

**Published:** March , 2019

### REFERENCES

1. "The History and Future of Plastics." *Science History Institute*, 20 Dec. 2016, [www.sciencehistory.org/the-history-and-future-of-plastics](http://www.sciencehistory.org/the-history-and-future-of-plastics).
2. Wright, Mike, *et al.* "The Stark Truth about How Long Your Plastic Footprint Will Last on the Planet." *The Telegraph*, 10 Jan. 2018, [www.telegraph.co.uk/news/2018/01/10/stark-truth-long-plastic-footprint-will-last-planet/](http://www.telegraph.co.uk/news/2018/01/10/stark-truth-long-plastic-footprint-will-last-planet/).
3. Jabeen, Nafisa, *et al.* "Bioplastics and Food Packaging: A Review." *Cogent Food & Agriculture*, vol. 1, no. 1, 2015, doi:10.1080/23311932.2015.1117749.
4. "Making a Plastic from Potato Starch." *Royal Society of Chemistry*, [www.rsc.org/Education/Teachers/Resources/Inspirational/resources/3.1.7.pdf](http://www.rsc.org/Education/Teachers/Resources/Inspirational/resources/3.1.7.pdf).
5. "Flame Test for Metal Ions." *BBC Bitesize*, [www.bbc.com/bitesize/guides/z9nr6yc/revision/1](http://www.bbc.com/bitesize/guides/z9nr6yc/revision/1).
6. Helmenstine, Anne Marie. "How Flame Test Colors Are Produced." [www.bbc.com/bitesize/guides/z9nr6yc/revision/1](http://www.bbc.com/bitesize/guides/z9nr6yc/revision/1).
7. "Daily Precipitation." *Central Weather Bureau*, [www.cwb.gov.tw/V7e/climate/dailyPrecipitation/dP.htm](http://www.cwb.gov.tw/V7e/climate/dailyPrecipitation/dP.htm).
8. "Advanced Topic: Oxidation Resistant Materials." *GA Sciences Education Foundation*, 2002, [www.sci-ed-ga.org/websites/gasef/images/pdf/light/section\\_13.pdf](http://www.sci-ed-ga.org/websites/gasef/images/pdf/light/section_13.pdf).

**Copyright:** © 2019 Tsai *et al.* All JEI articles are distributed under the attribution non-commercial, no derivative license (<http://creativecommons.org/licenses/by-nc-nd/3.0/>). This means that anyone is free to share, copy and distribute an unaltered article for non-commercial purposes provided the original author and source is credited.



# Combating insulin resistance using medicinal plants as a supplementary therapy to metformin in 3T3-L1 adipocytes

Diya Jayram<sup>1</sup> and Leya Joykutty<sup>1</sup>

<sup>1</sup> American Heritage School, Plantation, Florida

## SUMMARY

One in eleven people will have a form of diabetes during their lifetime (1). In 2012, diabetes and its life-threatening side effects cost 245 billion dollars in the United States (2). Averting type 2 diabetes (T2D) will significantly reduce health care costs and engender a healthier population. A primary cause of diabetes is insulin resistance, which is caused by disruption of insulin signal transduction. The objective was to maximize insulin sensitivity by creating a more effective, early intervention-based treatment to avert severe T2D. This treatment combined metformin, “the insulin sensitizer”, and medicinal plants, curcumin, fenugreek, and nettle. To conduct this study, insulin resistance was induced using free fatty acids (FFAs). Insulin sensitivity in adipocytes (propagated and differentiated from 3T3-L1 fibroblasts) was measured using assays specific for leptin concentration, glucose uptake, and Akt phosphorylation. These three proteins/pathways served as quantitative measurements for insulin sensitivity, since they are essential to insulin signaling. It was hypothesized that a dual therapy would maximize insulin sensitivity. This hypothesis was supported as each plant-enhanced combination treatment attenuated the effects of FFAs, increasing and reversing each biological marker of functional insulin signaling to normal function. This indicates that each treatment has the potential to combat obesity, augment glucose uptake, and heighten Akt/PI3K pathway function. This study, therefore, offers an improved multifunctional early intervention-based diabetes treatment that maximizes insulin sensitivity.

## INTRODUCTION

Diabetes, a devastating chronic disease, is one of the world’s rising problems. The number of people with diabetes has risen from 108 million in 1980, to 422 million in 2014 (1). In 2015, diabetes was the 7th leading cause of death in the United States. New cases are constantly being diagnosed: 1.5 million Americans are diagnosed with diabetes every year. Not only is it prevalent, but it is also a costly disease. In 2012, diabetes cost 245 billion dollars total in the United States (2). This study’s objectives were to discover a treatment that has the potential to prevent severe type 2 diabetes (T2D), reducing health care costs and saving lives.

T2D is a disease in which the body is incapable of responding to insulin, caused by damage or disruption in the

insulin signaling transduction system. Insulin signaling occurs when insulin binds to the tyrosine kinase insulin receptor (3). Leptin and insulin signaling converge at the level of IRS-PI 3-kinase (PI3K); therefore, they are closely related in glucose homeostasis (4). This convergence phosphorylates enzymes that activate the Akt/PI3K signaling pathway (5). The PI3K pathway plays essential functions in the cell, which includes lipid, protein, glycogen synthesis, and cell proliferation (6). The enzymes also activate GLUT4, which allows glucose to enter the cell by passive diffusion (7). Downstream metabolic enzymes break down glucose to generate ATP (**Figure 1**). Therefore, leptin, GLUT4, and Akt/PI3K were used as markers to measure insulin sensitivity. Furthermore, dysregulation of free fatty acid metabolism is a key event responsible for insulin resistance and T2D. (8). Therefore, free fatty acids (FFAs) were used to induce insulin resistance.

Prediabetes and mild T2D are commonly treated by metformin, an oral diabetes medicine that aids in preventing diabetes in people who are high risk and reduces the majority of diabetic complications (9). Metformin can restore leptin sensitivity, regulate GLUT4 translocation, and modulate Akt/PI3K pathway signaling. Curcumin, (10), fenugreek (11), and nettle (12) all have been proven to increase glucose uptake by the GLUT4 pathway, augment Akt phosphorylation by the Akt/PI3K pathway, and increase leptin concentration (10). Therefore, it was hypothesized that the synergistic effects of metformin and a medicinal plant may be able to reverse insulin resistance to a normal insulin sensitivity. The objective of this study was to examine the potential of the possible synergistic effects of medicinal plants (curcumin, fenugreek, and nettle) and metformin as an early intervention-based diabetes treatment to prevent diabetes and its complications, save lives, and reduce health care costs.

This objective was accomplished by propagating and differentiating 3T3-L1 adipocytes, inducing insulin resistance through free fatty acids (FFAs) (13), treating with the appropriate metformin and medicinal plant combination therapy, and measuring effectiveness/insulin sensitivity through significant protein and pathway markers in the insulin signal transduction system. The results accomplished by these methods demonstrated that this study offers a significantly more effective, multi-functional early intervention-based treatment for a costly, widespread disease: diabetes. Not only does this treatment combat diabetes, it also has the potential to combat obesity, another increasingly prevalent and destructive disease, by increasing leptin and attenuating

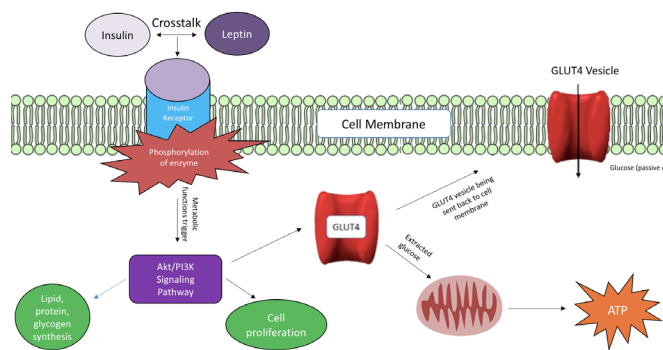


**Figure 1: Insulin Signal Transduction.** Simplified diagram conveying complex processes of insulin signal transduction that are significant to this study and explains the motive behind choosing leptin, GLUT4, and the Akt/PI3K pathways as biomarkers for measuring insulin sensitivity by describing the importance of the pathways to insulin signal transduction.

the effects of FFAs. Leptin, the appetite hormone, controls hunger, a symptom of diabetes; FFAs This paper also examines the effects of curcumin, fenugreek, and nettle on the insulin signal transduction system.

## RESULTS

To accurately measure insulin sensitivity, it was necessary to differentiate the preadipocytes before experimentation. Preadipocytes were cultured in T75 flasks and grew rapidly with proper adherence (**Figure 2A**). Preadipocytes were transferred to and differentiated in 12-well and 24-well plates successfully. Successful differentiation was signified by the presence of lipid droplets, observed as bright yellow spheres. The differentiated adipocytes accumulated yellow lipid droplets and had low adherence (**Figure 2B**). The Oil Red O assay was conducted to confirm differentiation and show clear presence of lipid droplets. The Oil Red O assay performed resulted in blue nuclei and bright red lipid droplets, demonstrating that differentiation was successful (Figure 2C). These differentiated cells were then treated with FFAs to induce insulin resistance and with combination therapies in an attempt to attenuate insulin resistance

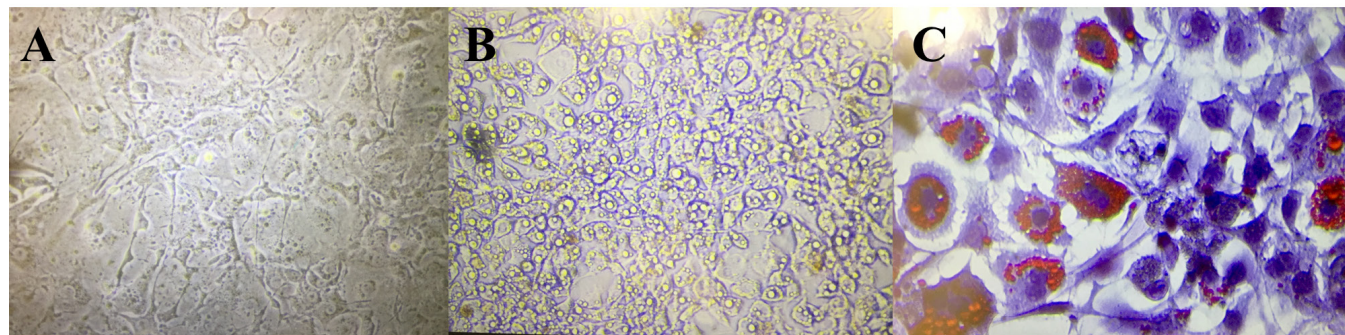


**Figure 2: Differentiation of 3T3-L1 Adipocytes** (A) 3T3-L1 preadipocytes prior to differentiation. (B) 3T3-L1 preadipocytes after differentiation prior to Oil Red O stain. Cells successfully differentiated, as depicted by the lipid droplets. (C) 3T3-L1 fully-differentiated adipocytes after Oil Red O Lipid Staining. Lipid droplets are stained red and nuclei are stained blue.

Treatment	Leptin (pg/mL)	Glut4 (pg/mL)	phospho-AKT (pg/mL)
Normal	45.98	240.02	14.58
Insulin-Resistant (IR)	40.89	213.44	10.00
Metformin (IR)	49.24	235.31	16.11
Curcumin	52.54	222.24	11.99
Curcumin (IR)	54.90	246.60	16.41
Curcumin w/ Metformin	57.63	338.86	21.36
Fenugreek	54.38	232.96	11.58
Fenugreek (IR)	52.10	247.08	17.81
Fenugreek w/ Metformin	68.57	313.65	25.12
Nettle	48.61	225.12	22.96
Nettle (IR)	54.20	256.05	24.45
Nettle w/ Metformin	65.77	286.58	38.20

**Table 1:** Raw quantitative results obtained from measuring leptin concentration, GLUT4 pathway function, and Akt phosphorylation.

To measure the efficacy at which the combination therapies attenuate insulin resistance, GLUT4, leptin, and Akt phosphorylation were measured using ELISAs specific to these markers. GLUT4, leptin, and Akt phosphorylation are significant in insulin signaling and are indicative of potential glucose uptake, hunger control, and Akt/PI3K function, respectively. Based on these markers, all combination treatments were effective at increasing insulin sensitivity (**Table 1**).

Curcumin ( $p=0.0110$ ), fenugreek ( $p=0.0041$ ), and nettle ( $p=0.0126$ ) combination treatments were each able to recover Akt levels (**Figure 3**). It was hypothesized that a dual therapy of a medicinal plant and metformin would restore the Akt concentrations to normal levels. The data show that each medicinal plant used with metformin produced an average Akt concentration higher than the normal value. The data also show that a nettle adjunct therapy is the most effective at enhancing Akt/PI3K pathway function because it produced the highest Akt concentration. Thus, curcumin, fenugreek,

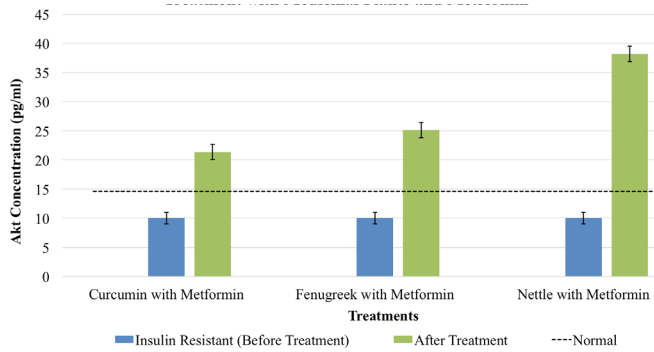


**Figure 3: Measurement of Akt phosphorylation in Adipocytes Following Treatment with Medicinal Plants and Metformin.** Bars represent the mean of phospho-Akt concentration of 4 samples. Error bars represent the standard deviation. The dashed line represents untreated/normal group. The dashed line acts as the baseline to measure treatment efficacy. \* indicates  $p < 0.05$  as determined by a Student's t-test. 1mM of metformin, 20  $\mu$ M of curcumin, 5  $\mu$ g/ml of fenugreek, and 5  $\mu$ g/ml of nettle was used.

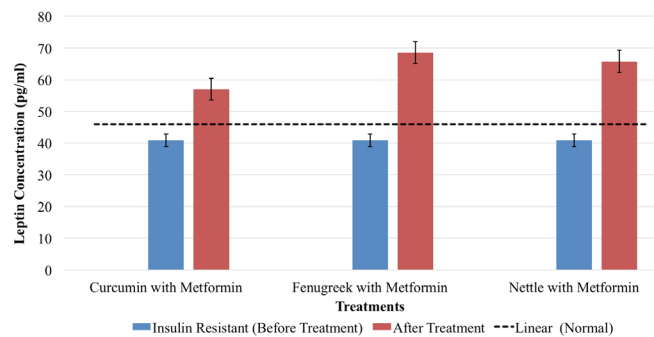


**Figure 4: Measurement of Leptin Concentration in Adipocytes Following Treatment with Medicinal plants and Metformin.** Bars represent the mean of leptin concentration of 4 samples. Error bars represent the standard deviation. The dashed line represents untreated/normal group. The dashed line acts as the baseline to measure treatment efficacy. \* indicates  $p < 0.05$  as determined by a Student's t-test. 1mM of metformin, 20  $\mu$ M of curcumin, 5  $\mu$ g/ml of fenugreek, and 5  $\mu$ g/ml of nettle was used.

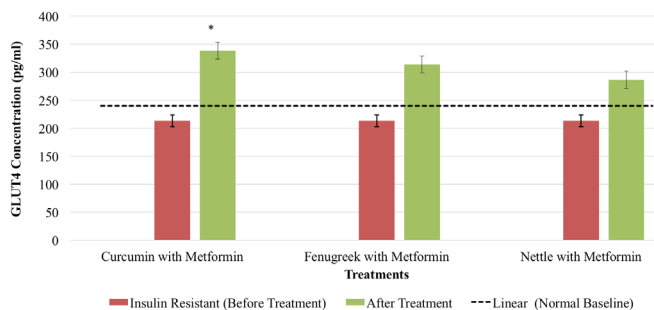


**Figure 5: Measurement of GLUT4 Concentration in Adipocytes Following Treatment with Medicinal plants and Metformin.** Bars represent the average of GLUT4 concentration of 4 samples. Error bars represent the standard deviation. The dashed line represents un-treated/normal group. The dashed line acts as the baseline to measure treatment efficacy. \* indicates  $p < 0.05$  as determined by a Student's t-test. 1mM of metformin (21), 20  $\mu$ M of curcumin, 5  $\mu$ g/ml of fenugreek, and 5  $\mu$ g/ml of nettle was used.

and nettle combination therapies were effective in maximizing Akt phosphorylation and attenuating the effects of free fatty acids (Figure 3), especially nettle, since Akt levels increased to match the normal baseline

Curcumin ( $p=0.0329$ ), fenugreek ( $p=0.0262$ ), and nettle ( $p=0.0072$ ) used as an adjunct therapy to metformin were each also able to significantly recover leptin levels (Figure 4). It was hypothesized that a dual therapy of a medicinal plant and metformin would restore leptin levels to normal concentrations. The data shows that each medicinal plant produced an average leptin concentration higher than the untreated group. The data also shows that a fenugreek supplementary treatment has the most potential to effectively satiate hunger as it produced the highest leptin concentration. Thus, curcumin, fenugreek, and nettle combination therapies were effective in maximizing leptin and attenuating the effects of free fatty acids (Figure 4), especially fenugreek, since leptin levels increased to match the normal baseline.

Curcumin ( $p=0.0093$ ), fenugreek ( $p=0.0387$ ), and nettle ( $p=0.0235$ ) as an addition to metformin were each able to recover GLUT4 levels, as well (Figure 5). It was hypothesized that a dual therapy of a medicinal plant and metformin would restore GLUT4 levels to normal concentrations. The data show that each medicinal plant used with metformin produced an average GLUT4 concentration higher than the normal values. A fenugreek adjunct therapy proved to be the most potentially effective at maximizing glucose uptake because it produced the highest GLUT4 concentration. Thus curcumin, fenugreek, and nettle combination therapies were effective in attenuating the effects of free fatty increasing GLUT4 levels to match the GLUT4 concentration before treatment with free fatty acids. All data was statistically significant based on a Student's t-test ( $\alpha=0.05$ ) and an ANOVA ( $\alpha=0.01$ ).

Using a medicinal plant with metformin maximized insulin sensitivity and produced synergistic effects (Figure 6). Each dual treatment produced an improvement in each biomarker's (leptin, GLUT4, and phospho-Akt) concentration when compared to the concentration of these biomarkers after treating with solely metformin. This controlled experimental setup directly attributes the improvement in insulin signal transduction biomarkers to the addition of medicinal plants. This showed that each adjunct treatment is more effective than only metformin at reversing insulin resistance. Fenugreek was the most effective at maximizing leptin (133.40%) and GLUT4 (129.70%) concentration, and nettle was the most effective at maximizing phosphorylated Akt concentration (237.11%). In fact, nettle doubled the efficiency of metformin as a diabetes treatment, in terms of the Akt/PI3K pathway.

## DISCUSSION

Diabetes, a chronic and costly metabolic disease, is one of the world's rising problems (14). Metformin, the current early-intervention based treatment, is usually used to treat severe prediabetes and mild T2D and is the go-to medication before insulin, but after other modifications, such as diet and

exercise, have been made.

The combination of metformin and the medicinal plants curcumin, fenugreek, and nettle have the potential to reduce constant hunger and combat obesity, augment glucose uptake, and heighten the Akt/PI3K pathway significantly more than solely metformin, therefore this experiment offers a more effective early-intervention diabetes treatment than solely metformin. This combination treatment is most applicable to the early stages of diabetes because these dual treatments improve an early-intervention-based drug, metformin. If diabetes is diagnosed in its early stages, this treatment could be utilized to return to a normal insulin sensitivity and avert severe T2D. In 2012, this disease cost the United States 245 billion dollars, and this number will only continue to increase because new cases are being diagnosed every day (2). Averting T2D will significantly reduce health care costs and engender a healthier population.

Furthermore, these dual treatments have the potential to combat obesity. Obesity leads to increased levels of circulating FFAs (fatty acids) that are converted into metabolites that induce insulin resistance (15). Restoring leptin levels maintain weight loss (16). This study offers a possible multi-functional treatment for obesity and diabetes by combatting the effects of FFAs and restoring leptin levels. Moreover, not much is currently known about fenugreek and nettle's efficacy in improving health condition, although these diet supplements are available across the world. This study offers new information on the effects of fenugreek, curcumin, and nettle in adipocytes.

This study could be further expanded to provide a more comprehensive perspective of the combination treatments' effects on insulin signaling: observing other important pathways in the insulin signal transduction system, such as IL-6, using different cell lines, utilizing other medicinal plants,

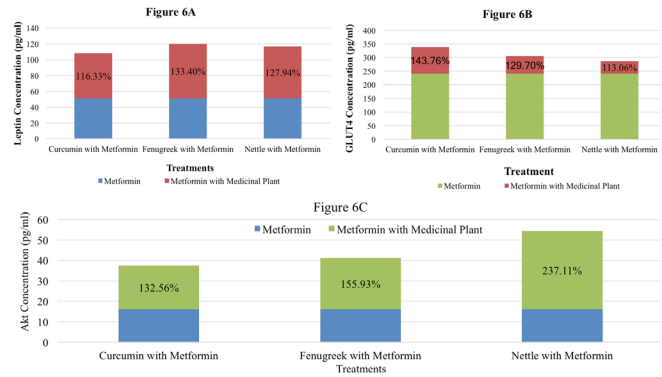


**Figure 6: Percent improvement After Medicinal Plant Addition to Metformin.** Compares the combination treatment groups with the metformin treatment group to show synergistic effects. The value on each bar shows the percent improvement of each adjunct treatment. Bottom bar represents treatment with solely metformin. Top bar represents the improvement that occurred with the addition of a medicinal plant.

and expanding to an animal model. Furthermore, metformin is currently being tested in cancer patients as a cancer prevention drug people at increased risk, including cancer survivors who have a higher risk of a second primary cancer, because of its association in the decrease of secondary cancers. (17). Curcumin (18), fenugreek (19), and nettle (20) have each been shown to be anticarcinogenic. This study could be expanded to observe how these dual treatments function as a cancer prevention therapy for cancer survivors who have a higher risk of a second primary cancer. In summary, this study offers a significantly more effective, multifunctional, insulin-sensitizing, early intervention-based treatment for diabetes, a costly, widespread disease.

Leptin						
Source of Variation	SS	dF	MS	F	P-value	F crit
Between Groups	2012.23	11	182.93	6.53	7.74 E-06	2.067
Within Groups	1008.87	36	28.02			
Total	3021.10	47				
GLUT4						
Source of Variation	SS	dF	MS	F	P-value	F crit
Between Groups	66580.7	11	5961.9	12.48	3.11 E-09	2.067
Within Groups	17199.8	36	477.77			
Total	82780.42	47				
Phospho-AKT						
Source of Variation	SS	dF	MS	F	P-value	F crit
Between Groups	2906.03	11	264.18	15.06	2.35 E-10	2.067
Within Groups	631.44	36	17.54			
Total	3537.47	47				

**Table 2:** Results of a one-way ANOVA conducted to analyze variance between and within groups. Differences between means of the treatment groups statistically significant ( $\alpha=0.01$ ).

## METHODS

3T3-L1 Mus musculus fibroblasts were cultured in complete preadipocyte medium (DMEM, supplemented with 10% BCS, 1% penicillin-streptomycin) in T75 flasks in a humidified incubator at 37°C with 5% CO<sub>2</sub>. All cell culture practices were conducted with good laboratory practices, with proper personal protective equipment, proper engineering controls, and within the parameters of the purchaser's chemical hygiene plan. All cell culture practices were performed under a cell culture laminar-flow hood. Preadipocytes were subcultured in a medium with 10% bovine calf serum and medium was changed every 2-3 days.

To prepare for differentiation, 3T3-L1 preadipocytes were transferred to 12-well and 24-well plates. Medium was replaced with fresh preadipocyte medium 48 hours prior to induction of differentiation. Differentiation was initiated at 80% confluency by replacing the preadipocyte medium with the differentiation medium (1.5 µg/ml insulin, 1 µM dexamethasone, 500 µM IBMX, and 1 µM rosiglitazone in DMEM:F12 (1:1) with 10% FBS). Differentiation medium was filter sterilized with a 0.22 µm syringe filter. Preadipocytes with differentiation medium were incubated for 3 days in a humidified incubator at 37°C with 5% CO<sub>2</sub>. Differentiated cells were maintained in maintenance medium (100 µl of a stock solution of insulin (1.5 mg/ml) was added to 100ml of DMEM/F12 (1:1) with 10% FBS). Maintenance medium was filter sterilized with a 0.22 µm syringe filter. Differentiation medium was removed and replaced with maintenance medium. Medium was changed every 2-3 days. Lipid droplet accumulation was visible by light microscopy 7-10 days after the addition of differentiation medium. Differentiation was confirmed using the Oil Red O Lipid Staining Kit (K580, BioVision). Cells were stained at a density of 0.1x10<sup>6</sup> in a 24 well plate. The presence of red stained lipid droplets indicated successful differentiation.

To induce insulin resistance, cells were treated with free fatty acids (FFAs). FFAs were prepared by dissolving 13.75 mg of palmitic sodium salt (Sigma Aldrich) in 600 µl MQ water (Sigma Aldrich) on a hot plate, heated and stirred till dissolved. 25 µl of dissolved FFA was added to 50 ml of maintenance medium. The solution was filter sterilized using a 0.22 µm filter. Combination treatments were made up of metformin and a medicinal. Metformin and each medicinal plant were dissolved in maintenance medium at different concentrations: 1mM of metformin (21), 20 µM of curcumin, 5 µg/ml of fenugreek, and 5 µg/ml of nettle. The treatments were administered to the cells according to the well plate diagram in **Figure XX**. Cell extracts were prepared for protein analysis. Cells were washed with pre-cooled PBS and a cell scraper was used to dissociate the cells. The cell suspension was transferred into a centrifuge tube. Suspension was centrifuged for 5 minutes at 1000xg. The medium was discarded and cells were washed 3 times with ice-cold PBS. The cell suspension was centrifuged for 10 minutes at 1500xg. Supernatants were aspirated and centrifuged at 1500xg for 10 minutes. The supernatants were used for the following assays. Akt quantification was carried

out on treated cells using an ELISA kit (ab126433, Abcam) according to the manufacturer's instructions. Quantification of GLUT4 was carried out on treated cells using an ELISA Kit (E-EL-M0564, Elabscience) according to the manufacturer's instructions. Quantification of leptin was carried out on treated cells using an ELISA Kit (ADI-900-019A, Enzo) according to the manufacturer's instructions.

The data collected was analyzed using a single factor ANOVA using Microsoft Office Excel (version 2016) with a significance level of  $\alpha=0.01$ . Once the one-way ANOVA showed a significant difference among the means of the treatments, a Student's t-test was used for each treatment to evaluate statistical difference between the treatments.

## ACKNOWLEDGEMENTS

Enzo Life Sciences provided the Leptin ELISA. Abcam provided a discount for the pSer472 phospho-Akt ELISA. Elabscience provided a discount for the GLUT4 ELISA. BioVision provided a discount for the 3T3-L1 Differentiation Kit and the Oil Red O Assay Kit.

**Received:** May 22, 2018

**Accepted:** November 5, 2018

**Published:** March 13, 2019

## REFERENCES

1. "Diabetes." World Health Organization, World Health Organization, 30 Oct. 2018, [www.who.int/news-room/fact-sheets/detail/diabetes](http://www.who.int/news-room/fact-sheets/detail/diabetes).
2. "The Cost of Diabetes." American Diabetes Association, [www.diabetes.org/advocacy/news-events/cost-of-diabetes.html](http://www.diabetes.org/advocacy/news-events/cost-of-diabetes.html).
3. Wang, Haitao, et al. "Proline-Rich Akt Substrate of 40kDa (PRAS40): A Novel Downstream Target of PI3k/Akt Signaling Pathway." *Cellular Signalling*, vol. 24, no. 1, 2012, pp. 17–24, doi:10.1016/j.cellsig.2011.08.010.
4. Kraus, Daniel, et al. "Leptin Secretion and Negative Autocrine Crosstalk with Insulin in Brown Adipocytes." *Journal of Endocrinology*, vol. 24, no. 1, 2002, pp. 185-91.
5. Kadota, Yoshito, et al. "Metallothioneins regulate the adipogenic differentiation of 3T3-L1 cells via the insulin signaling pathway." *PLOS One*, vol. 12, no. 4, 2017, doi: 10.1371/journal.pone.0176070.
6. Li, et al. "Silibinin Improves Palmitate-Induced Insulin Resistance in C2C12 Myotubes by Attenuating IRS-1/PI3K/Akt Pathway Inhibition." *Brazilian Journal of Medical and Biological Research*, vol. 48, no. 5, 2015, doi: 10.1590/1414-431X20144238.
7. Saini, Vandana. "Molecular Mechanisms of Insulin Resistance in Type 2 Diabetes Mellitus." *World Journal of Diabetes*, vol. 15, no. 3, pp. 68-75, doi: 10.4239/wjd.v1.i3.68.
8. Delarue, Jacques, and Christophe Magnan. "Free Fatty Acids and Insulin Resistance." *Current Opinion in Clinical Nutrition and Metabolic Care*, vol. 10, no. 2, pp. 142-48,

doi:10.1097/MCO.0b013e328042ba90.

10.3390/ijms19061547.

9. Nasri, Hamid and Mahmoud Rafieian-Kopaei. "Metformin: Current Knowledge." *Journal of Research in Medicinal Sciences*, vol. 19, no.1, 2014, pp. 658-664
10. Zhang, Dong-wei, et al. "Curcumin and Diabetes: A Systematic Review." *Hindawi*, 2013, doi: 10.1155/2013/636053.
11. Sundaram, Gopalakrishnan, et al. "Fenugreek, Diabetes, and Periodontal Disease: A Cross-Link of Sorts!" *Journal of Indian Society of Periodontology*, vol. 22, no. 2, 2018, pp. 122-126, doi: 10.4103/jisp.jisp\_322\_17.
12. Mahmoodnia, Leila, et al. "Traditional Uses of Medicinal Plants to Prevent and Treat Diabetes; An Updated Review of Ethnobotanical Studies in Iran." *Journal of Nephropathology*, vol. 6, no. 3, 2017, pp. 118-125, doi: 10.15171/jnp.2017.20.
13. Su, Li-qing, et al. "Effect Of Curcumin on Glucose and Lipid Metabolism, FFAs And TNF-a in Serum of Type 2 Diabetes Mellitus Rat Models." *Saudi Journal of Biological Sciences*, vol. 24, no. 8, 2017, pp. 17776-1780, doi: 10.1016/j.sjbs.2017.11.011.
14. Tanaka, Shiro, et al. "Cohort Profile: The Japan Diabetes Complications Study: A Long-Term Follow-Up Of A Randomised Lifestyle Intervention Study Of Type 2 Diabetes." *International Journal of Epidemiology*, vol. 43, no. 4, 2014, pp. 1054-1062, doi: 10.1093/ije/dyt057.
15. Aristizabal, Juan, et al. "Concentrations of Plasma Free Palmitoleic and Dihomo-Gamma Lin-oleic Fatty Acids Are Higher in Children with Abdominal Obesity." *Nutrients*, vol. 10, no. 1, 2018, doi: 10.3390/nu10010031.
16. Pala, Laura, et al. "The Therapy of Insulin Resistance in Other Diseases Besides Type 2 Diabetes." *Eating and Weight Disorders*, vol. 19, no. 3, 2014, pp. 275-283, doi: 10.1007/s40519-014-0139
17. Kasznicki, Jacek, et al. "Metformin in Cancer Prevention and Therapy." *Annals of Translational Medicine*, 2014, vol. 2, no. 6, 2014, doi: 10.3978/j.issn.2305-5839.2014.06.01.
18. Bachmeier, Beatrice E., et al. "The Role of Curcumin in Prevention and Management of Metastatic Disease." *International Journal of Molecular Sciences*, vol. 19, no. 6, 2018, doi: 10.3390/ijms19061716.
19. Shabbeer, Shabana et al. "Fenugreek: A Naturally Occurring Edible Spice as an Anticancer Agent." *Cancer biology & therapy*, vol. 8, no. 3, 2009, pp. 272-278
20. Fattahi, Sadegh, et al. "Nettle Inhibits Cell Growth and Induces Apoptosis by Targeting Ornithine Decarboxylase And Adenosine Deaminase As Key Regulatory Enzymes In Adenosine and Polyamines Homeostasis in Human Breast Cancer Cell Lines." *Cellular and Molecular Biology*, vol. 64, no. 3, 28 Feb. 2018, pp. 97-102, doi:10.14715/cmb/2018.64.3.16.
21. Chen, Dian et al. "Dual Effects of Metformin on Adipogenic Differentiation of 3T3-L1 Preadipocyte in AMPK-Dependent and Independent Manners" *International Journal of Molecular Sciences* vol. 19, no. 6, 2018, doi:

# Examining what causes perceived dissonance in musical intervals and the effect of timbre on dissonance

Michelle Hsu<sup>1</sup> and Hui-Yin Hsu<sup>2</sup>.

<sup>1</sup>Locust Valley High School, Locust Valley, New York.

<sup>2</sup>New York Institute of Technology, Old Westbury, New York.

## SUMMARY

Dissonance is perceived when certain musical notes are heard simultaneously and create a harsh, clashing feeling. Consonance, the opposite of dissonance, is perceived as a pleasant harmony of musical notes. Timbre is the defining characteristic of sound which differentiates sounds from different sources. This study attempts to determine the cause of perceived dissonance and the effect of timbre on dissonance. We attempt to corroborate Hermann von Helmholtz's theory of temporal dissonance, which proposes that dissonance results from beat frequencies created by interference of harmonic overtones. Our procedure examines algebraic and graphical representations of sound waves of the nine standard musical intervals from the minor second to the octave, produced on piano, ranging from dissonant to consonant. No clear correlations were found between different quantitative metrics and dissonance. The study also compares graphs of intervals from a piano and a human voice, which have different timbres. We noted that the graphs of piano notes, which have a "harder"-sounding timbre, had higher ratios of concavity changes to beat period than the graphs of sung notes, which have a "softer" timbre. Further research is planned to study whether graphical characteristics can reveal qualities of timbre.

## INTRODUCTION

Timbre is the tonal quality of sound. Unlike pitch or amplitude, timbre distinguishes a note on a piano from the same note on a violin. Timbre is perceived when the human brain interpretively fuses pure tones, or sinusoidal sound waves, that are at harmonic or nearly harmonic frequencies into one pitch known as a complex tone. The term "harmonic" refers to a harmonic series, a sequence of frequencies related to a fundamental frequency by whole number ratios (1). Each frequency in the sequence is a harmonic. Different instruments have different timbres due to the nature of their materials, such as strings or air columns. Although the same note or pitch played on each instrument has the same harmonic series, the relative loudness, or amplitudes, of the harmonics are different, thus creating distinct sound qualities for each instrument.

In music, combinations of two notes can be characterized by the musical intervals between the notes. These intervals are distinguished by comparing how dissonant they sound—that is, how harsh the notes are together. Consonance and dissonance can be described as the harmony and lack of harmony, respectively, between sounds and are easily and intuitively discernable by ear. Dissonant intervals are

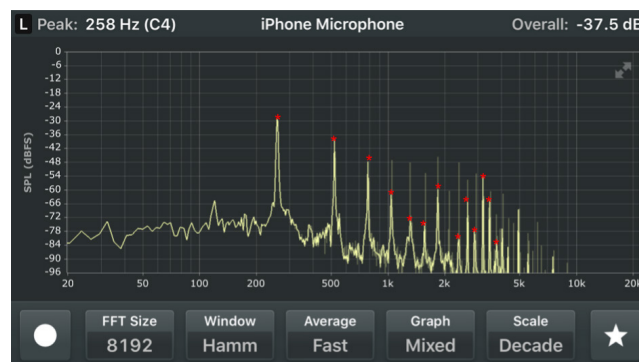


**Figure 1. Fourier analysis of C4 on piano.** On the piano used, the frequency of the note is 258 Hz rather than 261.626 Hz, which is likely due to the piano having gone slightly out of tune over time. The horizontal axis is frequency, in Hz, and the vertical axis is sound pressure level (SPL), in dBFS (decibels relative to full scale). dBFS is used in digital sound recordings, and full scale is the maximum loudness discerned by the device. dBFS describes the loudness of a sound relative to the full scale. Red asterisks denote the thirteen "peaks" for which frequency and SPL were recorded.

characteristically harsh-sounding, whereas consonant intervals are not. Hermann von Helmholtz's theory of temporal dissonance states that dissonance occurs when there is beating produced from harmonics of complex tones interfering with one another, with maximum dissonance produced at a beat frequency of around 35 Hz (hertz, cycles per second), and that dissonance is dependent on the magnitude of the interval between the pitches of the complex tones (2). Beat frequencies ranging from 10 to 60 Hz cause dissonance because the two frequencies producing it are too far apart to be registered as one pitch but too close to distinguish as distinct pitches (3). Because the relative amplitudes of harmonics for the same pitch but on different instruments are different, we hypothesized that the same intervals of pitches sounded from different instruments will be perceived as having different levels of dissonance.

Mathematician Joseph Fourier proved that all continuous functions can be broken up into an infinite number of sinusoidal waves (4). The Fourier Transform is able to break up a signal or waveform over time into the component sinusoids that make it up, representing the sinusoidal functions as graphs of amplitude against frequency (5). For complex tones, these frequencies are the fundamental frequency, which has the greatest amplitude, and its corresponding pure-tone harmonics. The study used the Fourier Transform to determine the equations for the most prominent pure tones of musical notes produced by different sources and analyze this information.

The aim of this study is to assess what causes perceived

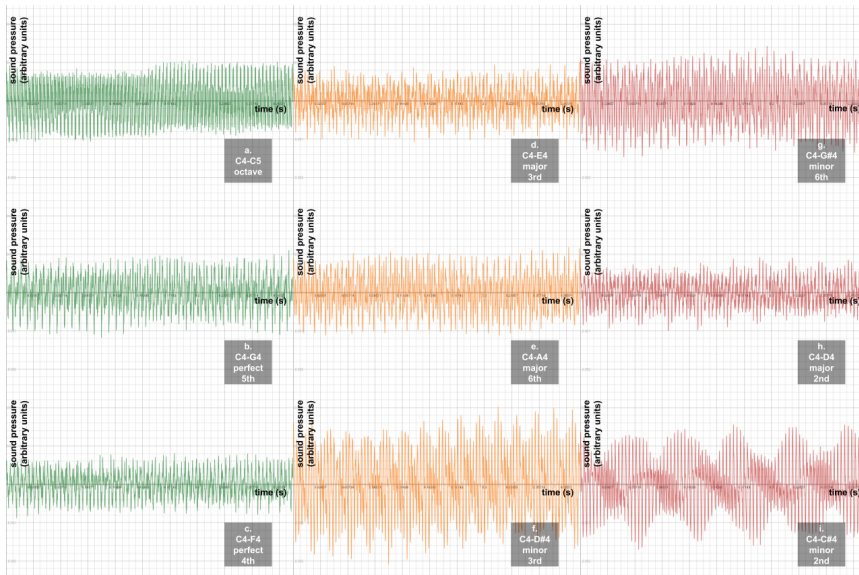


**Figure 2. Graphs of intervals.** These are not the original signals, but are equations representative of the sound waves created by summing sine waves with frequency and amplitude values derived from original signals. Played on piano ordered from least (top left; a) to most (bottom right; i) dissonant according to Helmholtz's theory. The horizontal axis of the graphs shows time elapsed in seconds, while the vertical axis shows the sound pressure except not to scale.

dissonance in musical intervals and whether timbre has an effect on dissonance. We hypothesized that Helmholtz's theory of temporal dissonance is correct. The experiment attempted to graphically and algebraically analyze dissonant intervals to corroborate Helmholtz's theory. This included examining the frequency of concavity changes in the graphs of sound waves as a possible determining characteristic of timbre, since adding sinusoidal functions of different frequencies and amplitudes results in different patterns of concavity. We also hypothesized that timbre affects perceived dissonance.

## RESULTS

We tested Helmholtz's theory of temporal dissonance by creating equations to represent the sound waves of intervals being played on a piano. We first generated equations representing the sound waves produced when individual notes are played on the piano by using a Fast Fourier Transform (FFT) smartphone application (Figure 1) (6) to obtain frequency and amplitude values for the component pure tones of each note. We then added these equations together to create graphs that represent two notes being played simultaneously (Figure 2). Each graph is of a different musical interval, with nine graphs in total representing the nine standard intervals between the minor second (C4-C#4) and the octave (C4-C5). All intervals had the lower note C4 and a higher note to produce the interval. For each interval, we calculated the number of beat frequencies between 10 and 60 Hz produced by the component frequencies of the notes in the interval, the observed beat frequency and period of the graph representative of the interval, the number of changes in concavity of the graph representative of the interval on  $0 \leq t \leq .3$  s, and the ratio of the number of changes in concavity to the beat period of the interval

$$\frac{\text{number of concavity changes in one beat period}}{\text{beat period}}$$

in order to examine what causes perceived dissonance in musical intervals. To find the number of beat frequencies between 10 and 60 Hz produced by the component frequencies of the notes in the intervals, we calculated the

beat frequencies produced by all combinations of component frequencies for each interval with the equation

$$\text{beat frequency} = |\text{frequency}_1 - \text{frequency}_2|$$

We counted the number of beat frequencies which were between 10 and 60 Hz for each interval. We found approximate beat frequencies and periods for the graphs representative of musical intervals by viewing the graphs in an online graphing program (7) and estimating the number of full cycles over a known time interval. If cycles were unclear, we adjusted the time interval until cycles became clear. We then calculated the beat frequencies in Hz with the equation

$$\text{beat frequency} = \frac{\text{number of cycles}}{\text{time in s}}$$

in Google Sheets. The beat periods in seconds were calculated by taking the reciprocals of the beat frequencies. To find the number of concavity changes in the graphs of the intervals, we created equations for the second derivatives of the equations for each interval. We graphed the second derivative equations and counted the number of horizontal axis crossings over the interval  $0 \leq t \leq 0.3$  s and over one beat period ( $0 \leq t \leq \text{beat period}$ ), which equals the number of

Interval (most to least dissonant)	Number of beat frequencies between component frequencies between 10 and 60 Hz	Beat frequency (Hz)	Beat period	Number of concavity changes over $t=0$ to $t=1/35$	Number of concavity changes in 1 beat period	Concavity changes/beat period
C4-C#4	3	1.75E+01	5.71E-02	1.33E+02	2.59E+02	4.53E+03
C4-D4	4	3.33E+00	3.00E-01	1.33E+02	1.41E+03	4.68E+03
C4-G#4	2	4.58E+00	2.18E-01	1.79E+02	1.31E+03	6.02E+03
C4-D#4	6	5.00E+01	2.00E-02	1.19E+02	8.10E+01	4.05E+03
C4-A4	0	6.67E+00	1.50E-01	1.55E+02	8.27E+02	5.51E+03
C4-E4	2	1.67E+00	6.00E-01	1.52E+02	3.09E+03	5.15E+03
C4-F4	0	2.78E+00	3.60E-01	1.43E+02	1.85E+03	5.13E+03
C4-G4	2	3.33E+00	3.00E-01	1.44E+02	1.56E+03	5.20E+03
C4-C5	2	2.50E+00	4.00E-01	1.61E+02	2.24E+03	5.60E+03

**Table1.** Table of calculated metrics for the nine musical intervals on piano. Intervals are ordered top to bottom from most to least dissonant according to Helmholtz's theory.



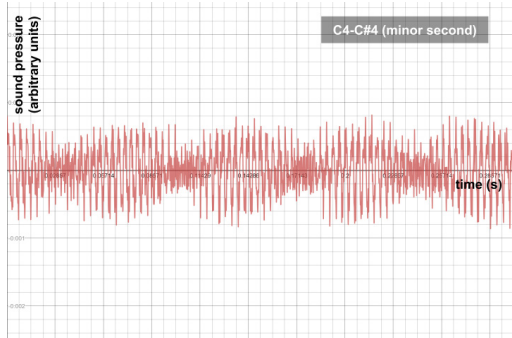


**Figure 3. Graph of C4-C#4 interval (minor second) played on piano.** This is not the original signal but rather an equation representative of the original signal created by summing sine waves with frequency and amplitude values derived from the original signal. The equation is not the sum of the equations for C4 and C#4.

concavity changes in the original equations. The intervals were ordered from least to most dissonant based on Helmholtz's theory of dissonance (1). There appeared to be no clear correlation between dissonance and the number of beat frequencies between 10 and 60 Hz produced by the component frequencies of the notes in the intervals, between dissonance and the observed beat frequency of the graph for the interval, between dissonance and the number of concavity changes in the graph for the interval over the same time interval ( $0 \leq t \leq 0.3$  s), or between dissonance and the ratio of concavity changes to the period of the observed beating for the equation of the interval (**Table 1**).

We conducted a control experiment to determine how similar the equations created by adding the equations for individual notes were to equations created for the sound wave of an interval. We created an equation representative of the sound wave produced by a C4 and C#4 played simultaneously on the piano. Visually, the control graph (**Figure 3**) is somewhat similar to the graph of the sum of the complex tone equations for C4 and C#4 (**Figure 2i**). We calculated the number of beat frequencies between 10 and 60 Hz produced by the component frequencies of the notes in the interval, the observed beat frequency and period of the graph representative of the interval, the number of changes in concavity of the graph representative of the interval on  $0 \leq t \leq 0.3$  s, and the ratio of the number of changes in concavity to the beat period of the interval. There are approximately four and a quarter beats within the interval  $0 \leq t \leq 0.3$  s in the control and approximately five and a quarter beats in the experimental results. Consequently, the beat frequency and period of the control graph and the summed graph (experimental) differ. The number of concavity changes over the same time interval and the ratios of concavity changes to beat periods also differ greatly between the control and sum graphs. However, the numbers of concavity changes in one beat period differ by only one, which is relatively small (**Table 2**). The numbers of beat frequencies between 10 and 60 Hz produced by component frequencies are equal. The discrepancies between the two graphs may be in part due to the C4 and C#4 not being played exactly simultaneously for the control graph, since the sum graph assumes the two notes are sounded at the exact same moment with no horizontal translation to account for a delay in the playing of one note. Despite the discrepancies, we chose to use the

summation of individual notes played separately rather than equations of intervals played directly so that the

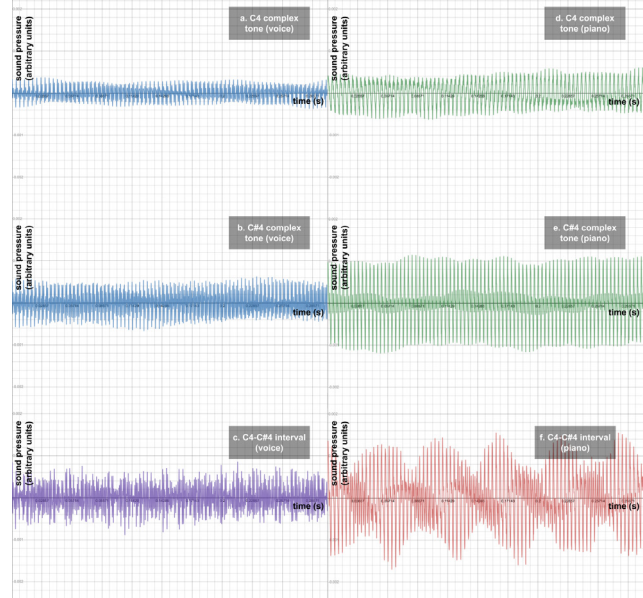


**Figure 4. Graphs of C4 and C#4 notes.** Not the original signals, but instead equations representative of the sound waves created by summing sine waves with frequency and amplitude values derived from original signals. C4-C#4 interval (minor second) created by adding the equations for the C4 and C#4 notes. Sung by voice (a, b, c) and played on piano (d, e, f).

bottom note in all intervals, C4, would have the same equation and serve as a controlled variable.

To determine what effect timbre has on dissonance, we compared a human voice to the piano. We created graphs of the notes C4 and C#4 and the C4-C#4 interval for both sources (**Figure 4**). We also created audio recordings of the C4-C#4 interval for both sources. Based on our perception by ear, the C4-C#4 interval sounded more dissonant on the piano than by voice. We concluded that timbre does affect perceived dissonance, affirming the hypothesis that the same interval sounded from different sources will be perceived as having different levels of dissonance. Individual notes sounded "harder" when played on piano than sung, which is a phenomenon difficult to describe in words.

Using the data processing pipeline outlined above, we analyzed the individual C4 and C#4 notes for piano and voice, as well as the C4-C#4 interval by voice (**Table 3**). For both C4 and C#4, the piano note graph had a higher ratio of concavity changes to beat period than the same note by voice (**Table 3**). For C4, the number of concavity changes over the same time interval and the number of concavity changes in one beat period are also lower for voice than for piano. However, for C#4, the number of concavity changes over the same time interval is higher for voice than piano, while the number of concavity changes in one beat period is the same for both piano and voice. For the C4-C#4 interval, the number of concavity changes over the same time interval and the ratio of concavity changes to beat period are higher for piano, and the number of concavity changes in one beat period is higher for voice. The number of beat frequencies between component frequencies between 10 and 60 Hz is the same for piano and voice. The values of the beat frequencies are also relatively

similar, which is expected because the

Interval	Number of beat frequencies between component frequencies between 10 and 60 Hz	Beat frequency (Hz)	Beat Period	Number of concavity changes over $t=0$ to $t=1/35$	Number of concavity changes in 1 beat period	Concavity changes/beat period
C4-C#4 sum	3	1.75E+01	5.71E-02	1.33E+02	2.59E+02	4.53E+03
C4-C#4 control	3	1.42E+01	7.06E-02	1.04E+02	2.58E+02	3.66E+03

**Table 2.** Table of calculated metrics for the representative equation of the C4-C#4 interval on piano created by summing representative equations for C4 and C#4 individually ("C4-C#4 sum", **Figure 1i**) and by recording FFT data for C4 and C#4 played simultaneously ("C4-C#4 control", **Figure 2**).

harmonic frequencies for the same note should be the same regardless of the note source.

### DISCUSSION

In this investigation, we hypothesized that Helmholtz's theory of temporal dissonance, which states that dissonance occurs when there is beating produced from harmonics of complex tones interfering with one another, with maximum dissonance produced at a beat frequency of around 35 Hz (hertz, cycles per second), and that dissonance is dependent on the magnitude of the interval between the pitches of the complex tones (2), is correct. We examined the nine standard musical intervals from the minor second to the octave. The musical interval from C4 to C#4 is a minor second because the notes are adjacent to each other on a piano with no key in between. To the ear, the two notes played simultaneously on the piano sound very dissonant because they are very close in pitch but perceptibly different, and there is a feeling of unresolved tension; according to Helmholtz's theory, the minor second is the most dissonant interval because the harmonics of the two pitches interfere to produce the most beat frequencies close to 35 Hz. The octave is the least dissonant (most consonant) interval according to Helmholtz's theory, with the frequencies of its two pitches related in a 1:2 ratio (one note's frequency is double that of the other). To the ear, two notes that are an octave apart sound like a high and low version of the same pitch. For example, imagine a grown man and a little girl singing the same note; most likely, they

Note/interval	Beat frequencies between component frequencies between 10 and 60 Hz	Frequency (Hz)	Period	Number of concavity changes over $t=0$ to $t=1/35$	Number of concavity changes in 1 beat period	Concavity changes/beat period
C4 piano	—	2.67E+02	3.75E-03	1.51E+02	2.10E+01	5.60E+03
C#4 piano	—	2.83E+02	3.53E-03	1.23E+02	1.70E+01	4.82E+03
C4 voice	—	2.50E+02	4.00E-03	6.60E+01	8.00E+00	2.00E+03
C#4 voice	—	2.75E+02	3.64E-03	1.38E+02	1.70E+01	4.68E+03
C4-C#4 piano	17, 32, 47	1.75E+01	5.71E-02	1.33E+02	2.59E+02	4.53E+03
C4-C#4 voice	17, 35, 56	5.67E+01	1.76E-02	1.18E+02	7.00E+01	3.97E+03

**Table 3.** Table of calculated metrics for C4 and C#4 notes. Not the original signals, but instead equations representative of the sound waves created by summing sine waves with frequency and amplitude values derived from original signals. C4-C#4 interval (minor second) created by adding the equations for the C4 and C#4 notes, on piano and by voice.

Frequency (Hz)	Sound Pressure Level (dBFS)	Amplitude	Frequency (trigonometric)	Component Equation	Complex Tone Equation
2.58E+02	-2.90E+01	3.55E-04	1.62E+03	$y=0.000355\sin(1620t) +$	$y=0.000355\sin(1620t) +$
5.19E+02	-3.78E+01	1.29E-04	3.26E+03	$y=0.000129\sin(3260t) +$	$0.000129\sin(3260t) +$
7.79E+02	-4.76E+01	4.17E-05	4.89E+03	$y=0.0000417\sin(4890t) + \dots$	$0.0000417\sin(4890t) + \dots$

**Table 4.** Shortened table of raw and manipulated data for C4 on piano. The full table contains data for thirteen frequencies, the first thirteen "peaks" in the FFT graph. Following the same structure, tables were created for the nine other piano notes used to create the nine intervals examined in this study.

will be singing one or multiple octaves apart; to bystanders, there would be no dissonance created from the two sounds. There are also intervals beyond the octave, but these were not included in this study.

We attempted to corroborate Helmholtz's theory by conducting graphical and algebraic analysis of musical intervals played on a piano passed through a Fast Fourier Transform. We did not find any clear correlations between dissonance and the number of beat frequencies between 10 and 60 Hz produced by the component frequencies of the notes in the intervals, between dissonance and the observed beat frequency of the graph for the interval, between dissonance and the number of concavity changes in the graph for the interval over the same time interval ( $0 \leq t \leq 0.3$  s), or between dissonance and the ratio of concavity changes to the period of the observed beating for the equation of the interval (**Table 1**). The results of the study do not conclusively support Helmholtz's theory of temporal dissonance.

We also hypothesized that timbre, the tonal quality of sound, has an effect on perceived dissonance. From listening by ear to the same interval (C4-C#4) from different sources (a piano and a human voice, in our case), we concluded that timbre does affect perceived dissonance. We examined the frequency of concavity changes in the graphs of sound waves as a possible determining characteristic of timbre, since adding sinusoidal functions of different frequencies and amplitudes results in different patterns of concavity. We repeated the graphical and algebraic analysis for intervals and individual notes played on a piano and sung by voice. Our results did not show consistent differences between notes and intervals sounded by voice and those played on piano. For the C4 note, the metrics for voice were consistently lower than the metrics for piano, but, for the C#4 note and C4-C#4 interval, some metrics were higher for voice, and some were higher for piano. To better examine whether the selected metrics are correlated to timbre, more notes and intervals should be tested, as well as more timbres.

In order to better draw conclusions regarding how sound waves interfere to produce dissonance and what could graphically signify dissonance, data and graphs for more different intervals should be gathered to determine a clearer trend. Intervals beginning with notes other than C4, as well as those beyond the octave, should be considered. As the control experiment indicated that the equations created by summing equations for individual notes differ from equations created from sounded intervals, it is a good idea to create equations from sounded intervals and conduct the same analyses and compare the results.

When we compared the same interval (C4-C#4) on piano and by voice, we found that the number of concavity changes over the same time interval and the ratio of concavity changes to beat period were higher for piano and that the number of concavity changes in one beat period was higher for voice. This may be related to timbre, but in order to investigate more thoroughly, it would be beneficial to create representative equations for complex tones produced by a variety of sources and examine whether there is a correlation between the ratio of concavity changes to beat period and “softness” in tonal quality. It would be interesting to investigate whether timbres can be discerned by graphical characteristics.

It should be noted that there are limitations in the data of this study. The selection of harmonic frequencies included in complex tone equations was done manually. At higher frequencies more distant from the fundamental frequency, it becomes harder to discern “peaks” by eye; thus, it is possible that some of the data taken were for frequencies other than harmonics, though these frequencies would be at lower amplitudes and therefore have less bearing on the shape of the complex tone graphs. For higher precision, one solution is to devise an algorithm to select “peaks” based on certain criteria. Another solution is to calculate the first twelve harmonic frequencies for each fundamental frequency and then refer to these values when recording FFT (Fast Fourier Transform) data. However, the calculated frequencies may not necessarily be “peaks”. In this study, we decided to record data for “peaks” because “peaks” are at relatively higher amplitudes than their neighboring frequencies and would therefore have more bearing on the shape of the resulting complex tone graphs. It would be helpful to repeat the process of collecting values several times and use the averages of these values to create equations and graphs. Imprecision was also introduced by the FFT application rounding frequency values to integers and SPL values to one decimal point. A different FFT application or software could allow for more precision.

Based on hearing alone, we can conclude that timbre does affect perceived dissonance, with “softer” timbres producing less dissonance than “harder” timbres for the same interval. This relationship could be corroborated by listening to the same interval played by many different instruments whose timbres would be qualified beforehand. This would require a system of classifying and describing timbres as well as many people to rate timbres and degrees of dissonance. This study could be carried out using the Internet to collect ratings from volunteers. Furthermore, intervals of two different instruments (in which one instrument plays one note and another plays another note) could be examined, which would allow a more thorough understanding of the effect of timbre on dissonance. Understanding how timbre affects perceived dissonance can improve the creation of new music, allowing composers to refine the characters of their music with careful selection of instruments in consideration of how their timbres will interact. One interesting aspect is the consideration of timbre in computer sound synthesis, which can both replicate the sounds of real instruments and produce completely new sounds that are not found naturally. Computer-synthesized sounds, as often heard in contemporary pop music, are a collection of more timbres to be explored. As a continuation of this study, we plan to study the graphs of complex tones of different sources in order to determine whether there is a

correlation between the ratio of concavity changes to beat period and “hardness” or “softness” in timbre.

In summary, the results of our study do not support Helmholtz’s theory of temporal dissonance. We did not find a clear relationship between perceived dissonance in a musical interval and the number of beat frequencies between 10 and 60 Hz produced by the component frequencies of the notes in the interval, the observed beat frequency of the graph for the interval, the number of concavity changes in the graph for the interval over the same time interval, or the ratio of concavity changes to the period of the observed beating for the equation of the interval. We concluded that timbre affects dissonance, and it appears that “softer” timbres create less dissonance than “harder” timbres. Our results suggest that the number of concavity changes over the same time interval, the number of concavity changes in one beat period, and the ratio of concavity changes to beat period may be correlated to timbre.

## METHODS

### Creating equations for component pure tones and complex tones

We used a Fast Fourier Transform (FFT) application (**Figure 1**) on a smartphone (6) to record the notes from C4 (frequency ≈ 261.626 Hz (8)) to C5 (frequency ≈ 523.251 Hz (8)), one octave higher than C4) on the piano. The frequencies and amplitudes for the first thirteen “peaks” in the graph (**Figure 1**) were recorded in tables to facilitate the creation of sine equations to represent the pure-tone sound waves at these frequencies. These peaks correspond to the fundamental frequency and twelve harmonics. Some imprecision is introduced because the application rounds the frequencies to integers and the loudness, or sound pressure levels, to one decimal point. The table below (**Table 4**), created in Google Sheets, displays the data recorded from the FFT graph (**Figure 1**) as well as amplitude and “trigonometric” frequency values that were calculated. To calculate the amplitude values, the equation

$$L = 20 \cdot \log\left(\frac{A}{A_0}\right)$$

was used, where L is the loudness in dBFS, A is the amplitude, and  $A_0$  is the reference amplitude which, for the purposes of this study, is arbitrarily assigned the value 0.01. The study is looking at the amplitudes proportional to one another, and the proportions will not be affected by the value of  $A_0$ . The value 0.01 was chosen after testing an online graphing program (7) and determining that, since the frequency values are large, zooming in would be required to view individual cycles of the sine waves, and so having small amplitudes for the equations would make the graphs easier to look at. Algebraically, assigning a smaller value to  $A_0$  causes A to have a smaller value. “log” denotes the common logarithm in base 10. The equation was manipulated to solve for A (each line of working is separated by a semi-colon).

$$L = 20 \cdot \log\left(\frac{A}{A_0}\right); \frac{L}{20} = \log\left(\frac{A}{A_0}\right); 10^{\frac{L}{20}} = \frac{A}{A_0}; .01(10^{\frac{L}{20}}) = A$$

The function tool in Google Sheets was used to calculate the amplitudes for each frequency. Since the frequencies from

the FFT application were given in Hz, they were converted to “trigonometric” frequencies, which represent the number of cycles in an interval of  $2\pi$  rather than 1. This way, the value of  $t$ , the independent variable of the sine equations to be created, equals the number of seconds elapsed rather than equaling the number of 12 seconds elapsed. An example of one conversion is below:

$$\frac{258 \text{ cycles}}{1 \text{ s}} = \frac{x}{2\pi \text{ s}}; x = 516\pi \text{ cycles}; \text{frequency} = 516\pi$$

The conversion of all frequency values was done with Google Sheets, yielding the values in the table. The frequencies listed in the table are not in terms of pi but have already been multiplied by pi to fourteen decimal places.

The sine equations representing pure tones were also created in Google Sheets. Then, the pure tone component equations were added to create an equation representing the resultant complex tone. Physically, when waves travel in the same position or space, they interfere with one another, so that the effects of the waves on the particles they travel through are compounded. This is known as superposition and can be represented mathematically by addition. For example, consider a wave displacing a particle  $p$  1 mm to the right. At the same instant, another wave is displacing particle  $p$  0.5 mm to the right. The effects of these two waves are added, so that the resulting displacement of particle  $p$  is 1.5 mm to the right.

### Creating graphs of musical intervals

The graphs for the nine musical intervals from a minor second to an octave (**Figure 2**) were produced by graphing the sums of the complex tone equations for C4 and a second note (For example, a perfect fifth is C4 and G4). The horizontal axis of the graphs shows time elapsed in seconds, while the vertical axis shows the sound pressure, or the additional pressure that a sound wave produces in propagating through a medium (9). To obtain the actual sound pressure values, each amplitude value must be multiplied by the actual reference amplitude ( $A_0$ ) and then by 100 to account for the arbitrarily assigned value of 0.01 to  $A_0$ . Because they would all be multiplied by the same factor, their proportions to each other would stay the same. The curves would also have to be shifted upwards so that there are no negative values for sound pressure.

### Control experiment

As a control experiment to determine the accuracy of the equations representing intervals produced by adding complex tone equations for individual notes, we recorded a C4 and C#4 played simultaneously on the piano with the FFT application and created an equation following the method described above. The first fourteen rather than thirteen “peaks” were recorded; since two notes are being played, there are two sets of a fundamental frequency and harmonics, so an even number is more suitable. “Peaks” could not be clearly identified visually beyond the first fourteen, so we did not record more “peaks”, though this would have increased the accuracy of the resulting equation created. The equation was graphed with the same online graphing program (7) (**Figure 3**).

### Finding the number of beat frequencies between 10 and 60 Hz in a musical interval

To obtain the data in Table 1 of the number of beat frequencies between 10 and 60 Hz in a musical interval, we used Google Sheets to calculate the beat frequencies produced by all combinations of component frequencies in the two notes of an interval for all nine intervals examined. The equation for calculating beat frequency is

$$\text{beat frequency} = |\text{frequency}_1 - \text{frequency}_2|$$

We highlighted and counted the beat frequencies which were between 10 and 60 Hz and recorded the values.

### Finding beat frequencies and periods for the graphs representative of musical intervals

To find approximate beat frequencies and periods for the graphs representative of musical intervals (**Table 1**), we visually estimated the number of full cycles over a certain time interval by examining the graphs in the online graphing program. If cycles were unclear, we adjusted the time interval until cycles became clear. We then calculated the beat frequencies in Hz with the equation

$$\text{beat frequency} = \frac{\text{number of cycles}}{\text{time in s}}$$

in Google Sheets. The beat periods in seconds were calculated by taking the reciprocals of the beat frequencies

$$\text{beat period} = \frac{1}{\text{beat frequency in Hz}}$$

### Finding the number of concavity changes in a graph representative of a musical interval and calculating the ratio of concavity changes to beat period

We calculated equations for the second derivatives of the equations representing musical intervals in Google Sheets using derivative rules. We then graphed these equations in the same online graphing program. We counted and recorded the number of horizontal axis crossings over  $0 \leq t \leq 0\text{cs}.3 \text{ s}$  for each graph. The number of horizontal axis crossings in a second derivative graph equals the number of concavity changes in the original graph representative of a musical interval, since the value of the second derivative at any point is the concavity of the original function at that point. We also counted and recorded the number of horizontal axis crossings over one beat period ( $0 \leq t \leq \text{beat period}$ ) for all musical intervals. We calculated a ratio of concavity changes to beat period for each musical interval with the equation

$$\text{ratio} = \frac{\text{number of concavity changes in one beat period}}{\text{beat period}}$$

These data are recorded in **Table 1**.

The data processing (excluding plotting) described above was also carried out for the equation from the control experiment.

### Comparing different timbres

To address the second part of the aim, “whether timbre has an effect on dissonance”, we recorded a human voice singing a C4 and C#4. The same procedure as above was followed. Video editing software (10) was used to overlay audio recordings of the C4 and C#4 notes so that they could be heard sounding simultaneously. The curves for C4

and C#4 by voice were added and the resulting curve was compared to the graph of the C4 and C#4 resultant for piano (Figure 4).

### Acknowledgements

The authors thank Shih-Chieh Hsu and Evangeline Papas for reviewing the manuscript and providing feedback.

**Received:** July 19, 2018

**Accepted:** January 02, 2019

**Published:** March 09, 2019

### REFERENCES

1. Bain, Reginald. "The Harmonic Series." University of South Carolina School of Music, in.music.sc.edu/.
2. Hartmann, Bill. "Consonance and Dissonance -Roughness Theory." Ohio State University School of Music, musiccog.ohio-state.edu/Music829B/roughness.html.
3. "5.5 Interference in Time: Beats." University of Connecticut, www.phys.uconn.edu/~gibson/Notes/Section5\_5/Sec5\_5.htm.
4. "Fourier Analysis and Synthesis." HyperPhysics, hyperphysics.phy-astr.gsu.edu/hbase/Audio/fourier.html#c1.
5. "Introduction to the Fourier Transform (Part 1)." Youtube, uploaded by Brian Douglas, www.youtube.com/watch?v=1JnayXHhjlg.
6. FFT Plot. Version 1.2.5, iPhone app, ONYX 3.
7. Graphing Calculator. Desmos, www.desmos.com/calculator/e1zIimpkc4I.
8. Szynalski, Tomasz P. "Online Tone Generator." Online Tone Generator, www.szynalski.com/tone-generator/.
9. "Acoustic Glossary." Acoustic Glossary, www.acoustic-glossary.co.uk/sound-pressure.htm.
10. iMovie. Version 10.1.1, MacBook app, Apple.

**Copyright:** © 2019 Hsu *et al.* All JEI articles are distributed under the attribution non-commercial, no derivative license (<http://creativecommons.org/licenses/by-nc-nd/3.0/>). This means that anyone is free to share, copy and distribute an unaltered article for non-commercial purposes provided the original author and source is credited.

# 3D Printed Polymer Scaffolds for Bone Tissue Regeneration

Nipun U. Jayatissa<sup>1</sup>, Sarit Bhaduri<sup>2</sup>

<sup>1</sup> Maumee Valley Country Day School, 1715 South Reynolds Road, Toledo, Ohio 43614-1499

<sup>2</sup> University of Toledo, Department of Mechanical Engineering and Surgery, 2801 W. Bancroft Street, Toledo, Ohio 43606

## SUMMARY

The regeneration of bone defects is a significant clinical challenge for patients around the world. The ideal scaffolds for bone tissue repair should provide biocompatibility, pore architecture, biodegradability, mechanical support, and cell attachment sites. Conventionally fabricated polymer scaffolds are still unable to make ideal scaffolds for bone tissue repair due to the lack of all the above mentioned properties. The investigated hypothesis was that increasing pore sizes of the scaffolds would cause an increase in the porosity and a decrease in the compressive modulus. In order to test the hypothesis, we designed three different pore sizes (200, 400, and 800  $\mu\text{m}$ ) in three different scaffolds using computer software. Relatively new 3D printing technology was used to print the three different types of porous scaffolds using polycaprolactone (PCL) polymer. These scaffolds were characterized for percent porosity, pore architecture, morphology, mechanical properties, and evaluated for biocompatibility and cell attachment with murine pre-osteoblasts. The percent porosity of these scaffolds (n=7) significantly increased from 13.31 to 61.66 (p<0.001) with the increase in pore size. The average compressive modulus of scaffolds (n=7) significantly decreased with the increase in pore size (p<0.001). The averaged compressive modulus of scaffolds with 200, 400, and 800  $\mu\text{m}$  pores is  $82.98 \pm 2.02$ ,  $61.60 \pm 2.59$ , and  $47.16 \pm 1.73$  MPa, respectively. In addition, PCL scaffolds show biocompatibility as determined by an *in vitro* cell study. These results have shown that the hypothesis is validated, and these 3D printed porous PCL scaffolds can be potentially used for bone regeneration applications. response teams and in developing areas.

## INTRODUCTION

The replacement or restoration of bone defects caused by trauma, fracture, and disease is a significant clinical challenge for both military and civilian patients (1-3). The bone has an intrinsic capacity to repair itself, which is best observed in the healing of bone fractures (4). However, when bone defects occur as a result of severe injury, healing may not commence spontaneously. Complicated pathological fractures or large defects need to be bridged using external intervention (5,6). Annually, the cost for bone fracture repair exceeds \$19 billion, and annual fractures and costs are projected to increase by 50% in 2025 (7).

There are two main types of bone grafts used in bone

fracture repair: autografts and allografts (8,9). These grafts provide the necessary mechanical and structural support during bone healing. Autograft bone tissue is taken from the patient's own healthy bone and implanted at the fractured site. Autograft contains viable cells, including new bone forming osteoblasts, supports the stability of the fractured site, and supports osteoblast function. However, the harvest site of autograft is subjected to injury due to the removal of the graft, and the patient undergoes donor site morbidity such as blood loss, infection risk, and scar formation. Allograft is taken from a cadaver and supports mechanical stability at the defect site and allows for cell attachment and cell function for surrounding cells (10). The two clinical drawbacks of the allograft are immunologic mismatch and risk of transmission of viral diseases.

Because of these clinical issues, scientists seek better methods for bone fracture healing, thus bone tissue engineering has emerged as a solution to treat bone fractures effectively and safely (11). In bone tissue engineering, one of the key elements is to create a resorbable or degradable scaffold, made of polymers, ceramics or polymer-ceramic composites (12), and bioactive glass (bioglass) (13,14). Bioglass has shown osteoconductivity, allows cells to attach to the surface of a material and promotes cell function. Bioglass has shown better osteoconductivity and therefore, polymer composite with bioglass have enhanced osteoconductivity compared to polymers alone. However, compared to polymers, the main drawback of bioglass is its inherent brittleness. Therefore, bioglass with polymer composite is used to prepare the scaffolds for bone regeneration to improve flexibility and reduce brittleness.

Scaffolds are three-dimensional (3D), biocompatible, and porous structures, which can mimic the extracellular matrix (ECM) properties including mechanical support, cellular activity, and protein production through biochemical and mechanical interactions. Bone is a load-bearing tissue, and in everyday life, compressive loading is the most common type of loading applied to bone (15). Therefore, it is important to know the compressive mechanical properties of scaffolds such as the compressive modulus. The ratio of applied compressive stress (force) to strain in the linear region is called compressive modulus (or stiffness). In addition, scaffolds provide sites for cell attachment, proliferation, differentiation, and stimulates bone tissue formation *in vivo* (12,16).

Pores in the scaffold are important for vascularization

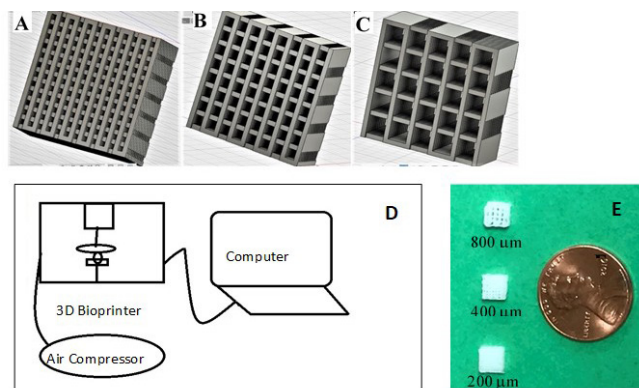


**Figure 1.** Cuboidal shaped porous PCL scaffold design created by computer software with three different pore sizes. (A) 200  $\mu\text{m}$ , (B) 400  $\mu\text{m}$ , (C) 800  $\mu\text{m}$ . (D) Sketch of 3D printing of scaffolds. (E) A picture shows visual appearance of printed PCL scaffolds with different pore sizes.

*in vivo*, which enables the transport of nutrients and waste-products in and out of the bone (6). Pore size and porosity are vital properties of a biomaterial scaffold for bone tissue regeneration, and large pore sizes and high porosity seems to enhance the *in vivo* bone ingrowth and osseointegration of the implant (17). The minimum recommended pore size for a scaffold should be between 100 and 150  $\mu\text{m}$  (6,17), but other studies have observed better osteogenesis when implants have larger than 300  $\mu\text{m}$  pore sizes. However, the increase in scaffold pore size results in reduced mechanical integrity of the scaffold.

Conventional polymer scaffolds are still unable to make ideal scaffolds for bone repair due to its poor mechanical properties, quick biodegradation, and inherent toxicity (18,19). In addition, current fabrication methods for polymer scaffolds use organic solvents, salts, and secondary containers to create the pores of the scaffolds. These additional materials may contribute contamination of the polymer scaffolds (12).

Relatively new 3D printing technology has emerged as a promising tool to fabricate patient specific 3D scaffolds with precise features since conventional scaffolds are unable to make ideal scaffolds for bone regeneration (18,19). This technology provides advantages compared to conventional fabrication methods including fabrication of versatile scaffolds with complex shapes, capability for homogeneous cell distribution, and mimicry of the ECM. 3D printing technology allows complex shapes of scaffolds to be printed with a bioink directly from a computer aided design (CAD) file. This technology is a branch of additive manufacturing which involves the process of sequentially adding layer upon layer of materials (12).

We investigated the hypothesis that increasing the pore size of the scaffolds would cause an increase in the porosity and a decrease in the compressive modulus. In this study, melted polycaprolactone (PCL) was used as a bioink to print the 3D porous scaffolds with a computer-controlled layer-by-layer addition process using extrusion printing. PCL is thermoplastic polyester and melts at 58-60°C. PCL degrades

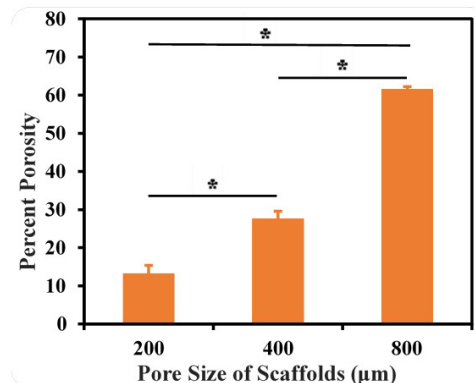


**Figure 2.** Percent porosity for three different porous PCL scaffolds. \* shows the statistically significant difference. Error bars represent the standard error of the data.

at a slower rate and is non-toxic. The Food and Drug Administration (FDA) approved the use of PCL related medical products such as sutures containing PCL and implantable contraceptive device (Capronor) (20). The use of PCL for drug delivery applications has also been approved by the FDA (21). To test the hypothesis, this paper focuses on the design and printing of 3D scaffolds with three different pore sizes (200  $\mu\text{m}$ , 400  $\mu\text{m}$ , and 800  $\mu\text{m}$ ); the characterization of scaffolds in terms of percent porosity, morphology, and mechanical properties; and the evaluation of scaffolds for cell (murine pre-osteoblast) viability, attachment, and proliferation.

## RESULTS

### Design and Printing of Scaffolds

To test the hypothesis, we made three different porous scaffold designs with the same dimensions and three different pore sizes (200, 400, and 800  $\mu\text{m}$ ) using computer software (Figure 1A-C). The scaffolds with 200, 400, and 800  $\mu\text{m}$  pore sizes took 25, 20, and 15 min, respectively, to completely print individually. The scaffold with small pores has more struts than the other two types of scaffold; therefore, it takes a longer time to print. Figure 1D shows the schematic representation of 3D printing the scaffolds, and Figure 1E shows the visual appearance of all three types of printed scaffold. The printed scaffolds all have the cuboidal shape similar to the original computer design of scaffolds (Figure 1D) with the same length (5 mm), width (5 mm), and thickness (2.4 mm).

### Percent Porosity of Scaffolds

The impact of different pore sizes on scaffold porosity was determined by calculating the percent porosity of the scaffolds. The numbers of pores in the scaffold increased with decreasing pore size. Scaffolds with 200, 400, and 800  $\mu\text{m}$  pores showed an average percent porosity ( $n=7$ ) of 13.31  $\pm$  2.06, 27.69  $\pm$  1.85, and 61.66  $\pm$  0.62, respectively (Figure 2). The percent porosity of scaffold significantly increased ( $p<0.001$ ) with the increase in pore size. The percent porosity of each group of scaffolds was significantly different ( $p<0.001$ ) when compared with the other two scaffold groups.

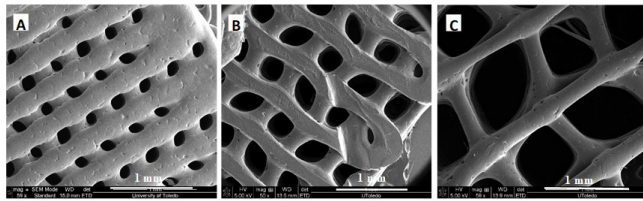


Figure 3. SEM images of three different porous PCL scaffolds. (A) 200 μm pores, (B) 400 μm pores, (C) 800 μm pores. Scale: 1 mm.

### Morphology of Scaffolds with SEM

The surface and pore morphology of scaffolds with different pore sizes were studied with SEM images (Figure 3). The images confirmed that the actual measured pore size of the scaffold increased with the designed increase in pore size. The original computer design of the scaffolds has square shaped pores in each type of scaffold groups. The pore morphology of 3D printed scaffolds with 400 and 800 mm pore sizes were approximately similar to the original cubical computer design. However, slightly smaller pore sizes were observed for scaffolds with original pore sizes of 200 and 400 mm. In addition, the struts of all three types of scaffolds were not straight as the original design.

### Mechanical Properties of Scaffolds

To test how different pore sizes impact the compressive modulus, the scaffolds were measured for mechanical properties. The stress-strain graph was generated for 200 μm pore scaffold, and the linear region was used to calculate the compressive modulus of the scaffold (Figure 4). The mean and standard error of the compressive modulus of the scaffolds are plotted in Figure 5. The average compressive modulus of the scaffolds (n=7) significantly decreased with the increase in pore size of the scaffold ( $p < 0.001$ ). We calculated the average compressive modulus for scaffolds with 200, 400

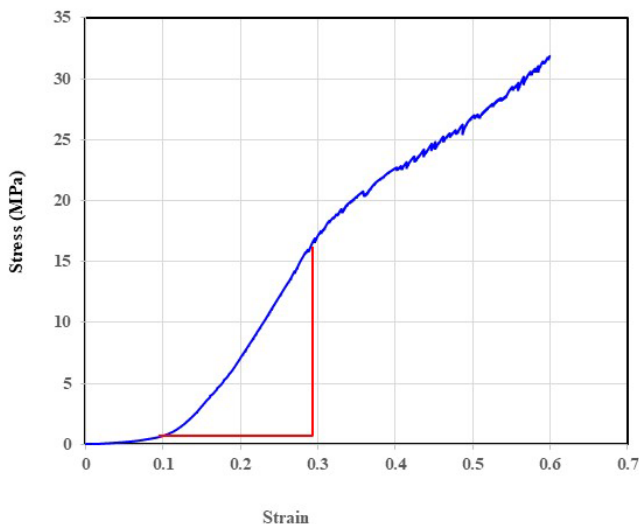


Figure 4. Stress-Strain plot for PCL scaffold used to calculate the compressive modulus. The slope was calculated using the distances in red in linear region.

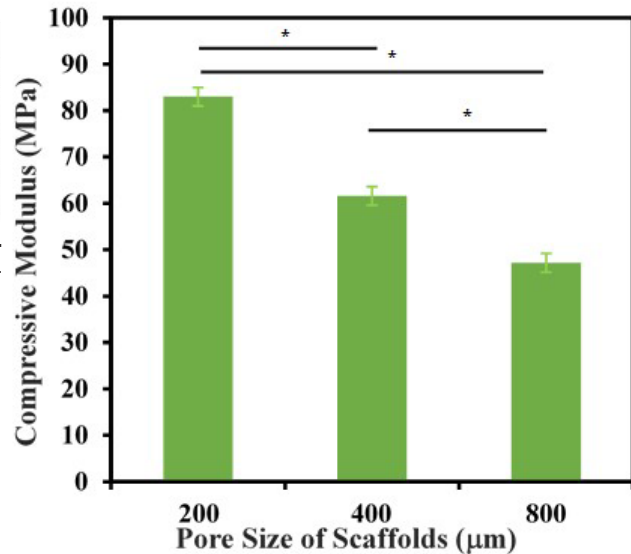


Figure 5. Compressive modulus for PCL scaffolds with three different pore sizes. \* shows the statistically significant difference. Error bars represent the standard error of the data.

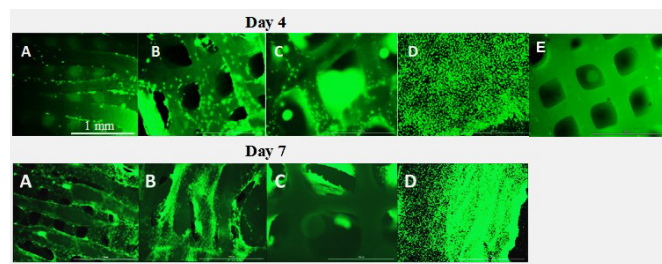


Figure 6. Fluorescent images for pre-osteoblasts cultured on PCL scaffolds at days 4 and 7 with three different pore sizes. (A) 200 μm, (B) 400 μm, (C) 800 μm, (D) control (without scaffold), (E) negative control image of a scaffold without cells. Scale: 1 mm.

and 800 μm pores to be  $82.98 \pm 2.02$ ,  $61.60 \pm 2.59$ , and  $47.16 \pm 1.73$  MPa, respectively. The compressive modulus of each scaffold types showed a significant difference ( $p < 0.001$ ) when compared to the two other types of scaffold.

### Cell Culture Studies In Vitro

The 3D printed scaffolds were qualitatively evaluated for cell attachment and viability using pre-osteoblasts at days 4 and 7 after cell seeding by visualizing cell attachment to the scaffolds (Figure 6). This result suggested that 3D printed PCL scaffolds permit cell attachment at days 4 or 7.

### DISCUSSION

The investigated hypothesis was that increasing the pore size of the scaffolds would cause an increase of the porosity and a decrease of the compressive modulus. In this study, 3D porous PCL scaffolds were designed with three different pore sizes (200, 400, and 800 μm) and directly printed using a melt extrusion 3D printing technique. The shape, size, and pore design of the 3D printed scaffolds (Figure 1E) were quite similar to the original designs. This technique of direct printing



did not require the use of organic solvents or salts to create the pores of the scaffolds. Therefore, this direct printing of PCL scaffolds avoids any possible contamination with any other secondary material or organic solvents.

The average percent porosity of the scaffolds significantly increased ( $p < 0.001$ ) with the increase in pore size of the scaffolds, so we accept our hypothesis (**Figure 2**). The percent porosity ranged from approximately 13.31 to 61.66 for the three types of scaffold. In this study, the pores of the PCL scaffolds were designed to mimic the natural human bone. The porosity of cortical bone and trabecular bone is in the range of 5% to 30% and 30% to 90%, respectively. Therefore, based on the results of the PCL scaffolds, they can be used to mimic either type of bone porosity.

The compressive modulus significantly decreased ( $p < 0.001$ ) with the increase in pore size of the scaffold. The average compressive modulus of the three types of PCL scaffolds ranged from 82.98 to 47.16 MPa (**Figure 5F**). The scaffolds with percent porosity of 13.31, 27.69, and 61.66 showed compressive moduli of 82.98, 61.6, and 47.16, respectively. Increasing the pore size of scaffolds reduced the compressive modulus, supporting the hypothesis. Previous studies have shown that the compressive modulus of PCL scaffolds with designed porosity between 37 and 55% is 52 to 68 MPa (22). Another study has shown that the compressive modulus of PCL is 6 MPa for PCL scaffolds with 55% porosity (23). Therefore, the compressive modulus of PCL scaffolds in this study is similar or higher compared to the reported values of previous studies (22). However, the porosity and compressive modulus of the scaffold should be balanced in order to have structurally strong scaffolds to serve for bone repair (24). The compressive modulus of cancellous bone is between 1-5000 MPa (25). Therefore, the PCL scaffolds printed in this study are potentially suitable to use for trabecular bone tissue regeneration.

PCL has shown minimal immune response when PCL devices were implanted for different medical applications (26,27). In addition, PCL devices have been approved by the FDA for medical applications (20). In vitro biocompatibility or cytotoxicity of materials can be evaluated using cell culture studies (28). In this study, cell attachment to the PCL scaffolds was used to determine whether cells were viable with all types of scaffolds (**Figure 6**). Previous studies have suggested that scaffolds with pore sizes in the range of 150-350  $\mu\text{m}$  are optimal for new bone formation, and pores larger than 400  $\mu\text{m}$  are favorable for vascularization (24). Based on the results, the scaffolds with 400  $\mu\text{m}$  pores would be better for future in vivo studies since these scaffolds have good mechanical properties and have large enough pores for cell growth. Although a test for scaffold degradation was not conducted in this study, the total degradation of PCL is reported to be 1.5-2 years (29). The degradation of PCL scaffolds can be accelerated with the increase of porosity in the scaffold. PCL degrades slowly in the body, allowing more structural support for growing cells for a longer period of time until dense tissue

forms. Another advantage of using PCL is that there are no adverse effects of their degraded products which feed into metabolic pathways (21).

The square-shaped pores and straight struts were designed in our original scaffold design. The scaffolds were printed using a computer design, thus theoretically scaffolds should be similar to each other. However, the SEM images showed slight differences in the measured dimensions of the pores as well as slight distortion of the shape of pores and straight lines. Particularly with the small pores, 200  $\mu\text{m}$ , this distortion was highly visible, and pores were slightly small when compared to the computer design's pore sizes in the scaffolds (**Figure 3**). This problem probably arises due to the lack of completely drying of the previously laid layer. Therefore, the new layer was laid down on to the previous layer distorted (or expanded), thus causing distortions. This problem could be avoided by drying the PCL layers as quickly as possible using a dryer or fan before adding the next layer. In this study, square-shaped pores were used. However, changing the pore geometry can be done by modifying the scaffold design; therefore, a scaffold could have squares or ovals. Modifying the shapes could have some impact on the porosity, mechanical properties, and/or cell function. In addition, the quantitative measurement of cell proliferation on the scaffolds can be assessed in the future using the MTS cell proliferation assay.

In conclusion, pre-designed PCL scaffolds with three different pore sizes were directly printed using a 3D printer. The printed scaffolds have shown the increased percent porosity with the increase in pore size of the scaffold. The compressive modulus of the three types of scaffolds increased with the decrease in the pore size of the scaffold. These results show that the hypothesis of this study is supported. In addition, these scaffolds permitted cell attachment as determined by cell culture studies at day 4 and day 7. These scaffolds have shown the reproducibility, biocompatibility, pore interconnectivity, porosity similar to bone, and compressive modulus similar to bone, and we observed viable cells on the scaffolds. Therefore, these PCL scaffolds can be potentially used to regenerate or repair bone defects.

## MATERIALS AND METHODS

### Materials

PCL Pellets (molecular weight 50,000 Da) were purchased from BioBiotics Inc. (USA). Alpha minimum essential medium ( $\alpha$ -MEM), phosphate buffered saline (PBS), penicillin/streptomycin and fetal bovine serum (FBS), and 0.25% trypsin-EDTA phenol red were all purchased from Gibco (USA). Live/dead cell viability/cytotoxicity kit were purchased from Invitrogen (USA).

### Design and Printing of 3D Porous PCL Scaffolds

Three different types of 3D porous scaffolds with pore sizes 200, 400, and 800  $\mu\text{m}$  were designed and drawn using

Autodesk Fusion 360 software (**Figure 1A**). The dimensions of these cuboid 3D scaffolds were designed with a length of 5 mm, a width of 5 mm, and a thickness of 2.2 mm. Each scaffold was designed to have 22 layers with 100  $\mu\text{m}$  thickness of each layer in the z direction. A commercial bioprinter, BioBots (BioBots Inc., Philadelphia, PA, USA) with computer driven x-y-z moving system attached nozzles was used to print 3D scaffolds by extrusion printing with layer-by-layer process. An air compressor was attached to regulate the pressure of the extruded bioink in the printing system. The PCL pellets were loaded into the metal syringe attached to extruder and melted at 100°C with pressure at 100 PSI.

### Percent Porosity of Scaffolds

The total volume of each of the three types of cuboid shaped scaffolds (Total volume = length x width x thickness) was calculated by measuring the length, width, and thickness of each scaffold using a Vernier caliper (n=7). The volume of solids of each scaffold was calculated by measuring the mass of each group of scaffolds (n=7) and dividing it by the density of PCL (1.1 g/cm<sup>3</sup>). The percent porosity of scaffolds (n=7) from each of the three types of scaffold groups was calculated using the following equation:

$$\text{Percent Porosity} = \left( \frac{\text{Volume of Pores}}{\text{Total Volume}} \right) \times 100\% = \left( \frac{\text{Total Volume} - \text{Volume of Solids}}{\text{Total Volume}} \right) \times 100\%$$

### Morphology of Scaffolds with Scanning Electron Microscope (SEM)

The surface and pore morphology of scaffolds (n=3) were observed using SEM (FEI quanta 3D FEG, FEI Company, Hillsboro, OR, USA). Since PCL is not conductive, scaffolds were sputter coated with gold for 30 seconds using a sputter coater.

### Test of Mechanical Properties of Scaffolds

The mechanical properties of the scaffolds were conducted using ADMET eXpert 2600 series (ADMET, Inc., Norwood, MA, USA) Universal mechanical testing machine. One scaffold was placed on the middle of the flat smooth steel fixture. Scaffolds from each group (n=7) were compressed by the flat stainless steel crosshead with Interface SM-250 load cell with the rate of 0.01 mm/s. Force on the load transducer against crosshead position graph was generated by ADMET's MTESTQuatro software. Then these data were used to produce stress-strain graph in excel file. Stress and strain of scaffold can be defined as follows:

Stress = Force/bottom or top surface area of the scaffold

Strain = Change of thickness in z-direction/original thickness of the scaffold

The compressive modulus of the scaffold was calculated from the slope of the linear region (elastic region) of the stress-strain graph, for each of the three types of scaffolds.

### Cell Culture Studies In Vitro

PCL scaffolds (n=3 per each type of scaffold) were

sterilized with Ultra Violet (UV) light for 30 min in 24-well plate. Next, murine pre-osteoblasts (Sigma) were seeded on top of the scaffolds with cell density of 40,000 cells/well using a medium of alpha minimum essential medium ( $\alpha$ -MEM) combined with 15% fetal bovine serum (FBS) and 1% penicillin/streptomycin. The pre-osteoblasts seeded scaffolds in 24-well plate were incubated in 5% CO<sub>2</sub>/95% air incubator at 37°C. Culture medium was changed every 2-3 days until scaffolds were used for the testing at day 4 and 7. Another 24-well plate without scaffold was seeded with the cell density of 40,000/well and used as a control (n=3). Cell seeded three types of scaffolds were transferred to new 24-well plate prior to do the Live/Dead cell assay. Cell viability was determined by the use of a green fluorescence dye, calcein, and dead cells were shown through the use of a red fluorescence dye ethidium homodimer-1. Cell viability on scaffolds were imaged using a fluorescence microscope.

### Statistical Analysis

For porosity and mechanical testing of scaffolds (n=7 scaffolds per group) were used and the mean  $\pm$  standard error was calculated and plotted in the graphs. The IBM SPSS Statistics version 21 software was used to compare porosity and compressive modulus data of the three scaffold groups using one-way analysis of variance (ANOVA) with 99.9% confidence interval followed by Tukey Post Hoc multiple statistical comparison procedure. Differences were considered significant if p < 0.001.

### ACKNOWLEDGEMENT

The first author would like to thank the University of Toledo for allowing him to use the facilities to conduct the experiments in this project.

**Received:** July 26, 2018

**Accepted:** January 18, 2018

**Published:** April 28, 2019

### REFERENCES

1. Pollak, A. N. "Timing of debridement of open fractures." *Journal of the American Academy of Orthopaedic Surgeons*, vol. 14, no. supplement 10, 2006, pp. S48-51.
2. Clarke, B. "Normal bone anatomy and physiology." *Clinical Journal of the American Society of Nephrology*, vol. 3, no. supplement 3, 2008, pp. S131-39.
3. Giannotti, S., *et al.*, "Current medical treatment strategies concerning fracture healing." *Clinical Cases in mineral and bone metabolism*, vol. 10, no. 2, 2013, pp. 116-20.
4. Kon, E., *et al.*, "Bone regeneration with mesenchymal stem cells." *Clinical Cases in mineral and bone metabolism*, vol. 9, no. 1, 2012, pp. 24-27.
5. Seitz, H., *et al.*, "Three-dimensional printing of porous ceramic scaffolds for bone tissue engineering." *Journal of Biomedical Materials Research Part B*. vol. 74, no. 2, 2005, pp. 782-88.

6. Jones, A. C., *et al.*, "Assessment of bone ingrowth into porous biomaterials using MICRO-CT." *Biomaterials*, vol. 28, no. 15, 2007, pp. 2491-04.
7. Burge, R., *et al.*, "Incidence and economic burden of osteoporosis-related fractures in the United States, 2005-25." *Journal of Bone and Mineral Research*, vol. 22, no. 3, 2007, pp. 465-75.
8. De Long, W. G., *et al.*, "Bone grafts and bone graft substitutes in orthopaedic trauma surgery. A critical analysis." *Journal of bone and joint surgery. American volume*, vol. 89, 2007, pp. 649-58.
9. Khan, Y., *et al.*, "Tissue engineering of bone: Material and matrix considerations." *Journal of bone and joint surgery. American volume*, vol. 90, no. supplement 1, 2008, pp. 36-42.
10. Boyce, T., *et al.*, "Allograft bone. The influence of processing on safety and performance." *Orthopedic Clinics of North America*, vol. 30, no. 4, 1999, pp. 571-81.
11. Khademhosseini A., *et al.*, "Progress in tissue engineering." *Scientific American*, vol. 300, no. 5, 2009, pp. 64-71.
12. Bose, S., *et al.*, "Bone tissue engineering using 3D printing." *Materials Today*. vol. 16, no. 12, 2013, pp. 496-04.
13. Misra, S. K., *et al.*, "Poly(3-hydroxybutyrate) multifunctional composite scaffolds for tissue engineering applications." *Biomaterials*, vol. 31, no. 10, 2010, pp. 2806-15.
14. Vergnol, G., *et al.*, "In vitro and in vivo evaluation of a polylactic acid-bioactive glass composite for bone fixation devices." *Journal of Biomedical Materials Research Part B*, vol. 104, no. 1, 2016, pp. 180-91.
15. Zhou, Z., *et al.*, "Development of three-dimensional printing polymer-ceramic scaffolds with enhanced compressive properties and tuneable resorption." *Materials Science and Engineering C*, vol. 93, 2018, pp. 975-86.
16. Rezwana, K., *et al.*, "Biodegradable and bioactive porous polymer inorganic composite scaffolds for bone tissue engineering." *Biomaterials*, vol. 27, no. 18, 2006, pp. 3413-31.
17. Karageorgiou, V., and Kaplan, D. "Porosity of 3D biomaterial scaffolds and osteogenesis." *Biomaterials*, vol. 26, no. 27, 2005, pp. 5474-91.
18. Jeong, C. G., and Atala, A. "3D Printing and Biofabrication for Load Bearing Tissue Engineering." *Advances in Experimental Medicine and Biology*, vol. 881, 2015, pp. 3-14.
19. Hollister, S. J., *et al.*, "Design control for clinical translation of 3D printed modular scaffolds." *Annals of Biomedical Engineering*, vol. 43, no. 3, 2015, pp. 774-86.
20. Li, Z., and Tan, B. H. "Towards the development of polycaprolactone based amphiphilic block copolymers: molecular design, self-assembly and biomedical applications." *Materials Science and Engineering C*, vol. 45, 2014, pp. 620-34.
21. Woodruff, M. A., and Hutmacher, D. W. "The return of a forgotten polymer-Polycaprolactone in the 21st century." *Progress in Polymer Science*. vol. 35, no. 10, 2010, pp. 1217-56.
22. Williams, J. M., *et al.*, "Bone tissue engineering using polycaprolactone scaffolds fabricated via selective laser sintering". *Biomaterials*, vol. 26, no. 23, 2005, pp. 4817-27.
23. Cahill, S., *et al.*, "Finite element predictions compared to experimental results for the effective modulus of bone tissue engineering scaffolds fabricated by selective laser sintering." *Journal of Materials Science: Materials in Medicine*, vol. 20, no. 6, 2009, pp. 1255-62.
24. Bose, S., *et al.*, "Recent advances in bone tissue engineering scaffolds." *Trends in Biotechnology*, vol. 30, no. 10, 2012, pp. 546-54.
25. Olszta, M. J., *et al.*, "Bone structure and formation: A new perspective." *Materials Science & Engineering R: Reports*, vol. 58, no. 3-5, 2007, pp. 77-116.
26. Petrigliano, F. A., *et al.*, "In vivo evaluation of electrospun polycaprolactone graft for anterior cruciate ligament engineering." *Tissue Engineering Part A*, vol. 21, no. 7-8, 2015, pp. 1228-36.
27. Nyitray, C. E., *et al.*, "Polycaprolactone Thin-Film Micro- and Nanoporous Cell-Encapsulation Devices." *ACS Nano*. vol. 9, no. 6, 2015, pp. 5675-82.
28. Williams, D. F. "On the mechanisms of biocompatibility". *Biomaterials*, vol. 29, no. 20, 2008, pp. 2941-2953.
29. Sun, H., *et al.*, "The in vivo degradation, absorption and excretion of PCL-based implant". *Biomaterials*, vol. 27, no. 9, 2006, pp. 1735-40.

# Cytokine treatment for myocarditis may directly impact cardiomyocytes negatively

Jacob Kasner<sup>1</sup> and Leya Joykuty<sup>1</sup>

<sup>1</sup>American Heritage School, Plantation, Florida

## SUMMARY

The purpose of our study was to determine if direct administration of CXCL1/KC to cardiomyocytes causes negative changes to cell density or proliferation. This molecule has been shown to reduce inflammation in certain instances. Homocysteine models the direct effect of an inflammatory agent on cardiomyocytes. Our question was whether these molecules directly impact cell density through an interaction with the cell proliferation process. We hypothesized that cells treated with CXCL1/KC would maintain the same cell density as untreated cells. In contrast, cells treated with Homocysteine or both Homocysteine and CXCL1/KC, were expected to have a higher cell density than that of untreated cells. To test these hypotheses, HL-1 cardiomyocytes were cultured and treated in chambers on a glass slide. DAPI staining, which allows individual nuclei to be counted, was viewed under fluorescence and pictures were analyzed using Image J. Our hypotheses were rejected because there was a significant difference between the Homocysteine group and both the Homocysteine+CXCL1/KC and CXCL1/KC groups. This was extended to signify that the cell density of the CXCL1/KC and Homocysteine+CXCL1/KC groups was decreased cell proliferation had been reduced. The difference between the CXCL1/KC and Homocysteine groups likely indicates effects possessed by each treatment. Comparing results from the Homocysteine+CXCL1/KC treatment to the Homocysteine treatment, Homocysteine treatment increased cell density enough so that the decreased proliferation which may have been caused by the CXCL1/KC was significant compared to the Homocysteine sample. Future studies could examine additional applicable models such as mouse heart tissue or a living mouse.

## INTRODUCTION

In general, inflammation is not a disease and can be beneficial in the healing process. For example, the inflammatory process is crucial when responding to an infection. In the most basic sense, it is the action of the immune system flooding the affected area with blood, fluid, and proteins that create swelling and heat to heal the damage. The impact of inflammation occurs at the cellular and organ system levels (1). The immune system begins the inflammatory

process when sentinel cells signal to macrophages, B-cells, and T-cells that will directly address the infection. As this is occurring, the cardiovascular system leaks plasma from its capillaries to slow down the infection (1). This process indirectly involves cardiomyocytes. The issue arises when there is a constant low-level of inflammation caused by a hyperactive immune system that can result in myocarditis.

Myocarditis is an inflammatory disease of heart muscle. One of the most common causes for the disease is viral infection (2). Despite not being as widely known as atherosclerosis or tuberculosis, myocarditis is one of several diseases that threatens many members of today's society. Furthermore, myocarditis is known to cause dilated cardiomyopathy, which is more serious and better-known (3). According to one study, dilated cardiomyopathy can be defined as a loss of function in one or both ventricles and dilation that cannot be explained through the presence of other conditions such as coronary artery disease (4). In simpler terms, the disease encompasses the full or partial loss of contraction in at least half of the heart, as well as the enlargement of heart muscle. This loss of function can lead to blood clots, heart failure, or even sudden death. All these effects are consequences of the inflammatory process.

Myocarditis is difficult to diagnose because it presents with symptoms such as chest pain, shortness of breath, and abnormal rhythms which can be indicative of other cardiovascular diseases (5). As a result, many cases go undiagnosed. For some variants of myocarditis, there is less than a 20% chance of survival due to underdiagnosis and lack of treatment (5). Currently, the accepted treatment for myocarditis is immunosuppressive therapy, which has succeeded in improving the quality of life of afflicted patients (6). However, this treatment brings down the walls of protection that patients previously had against familiar pathogens like the common cold. Due to this, otherwise harmless infections can be lethal for immunosuppressed patients. To circumvent this issue, identifying another method of treatment would be ideal. Considering their expansive role in the immune system, we hypothesized that cytokines could be a potential treatment.

Many cytokines are known to have roles in the inflammation pathway. These cytokines are typically involved in the recruitment of neutrophils to increase inflammation. Chemokines, a variant of cytokines, interact with receptors to activate intracellular signaling pathways. Many of them recruit monocytes and are thus pro-inflammatory in nature. CXCL1/

KC is a chemokine that is not pro-inflammatory; rather it blocks antibodies and increases neointimal formation, reducing inflammation. CXCL1/KC was found to abrogate inflammation of cardiac muscle cells (7). Other researchers that have worked with CXCL1/KC in the context of the cardiovascular system have shown that 100 nmol of the cytokine is a physiologically relevant dose (personal communication). CXCL1/KC has been found to have the opposite effect on cardiac muscle cells. CXCL1/KC belongs to a group of cytokines known as inflammatory cytokines. These molecules have recently piqued the interest of the cardiovascular research field. They are now known to be involved in the development of diseases such as atherosclerosis, the cardiac dysfunction in systemic sepsis, and viral myocarditis (8).” Homocysteine was recognized as a risk factor for the presence of atherosclerotic vascular disease and hypercoagulability states in the early 1990s due to its molecular products, superoxide and hydrogen peroxide (9). Homocysteine causes oxidative damage to endothelial cells, the cells that line the walls of the blood vessels. The presence of increased levels of hydrogen peroxide recruits monocyte infiltration in vascular smooth muscle cells, contributing to vascular inflammation (10). Superoxide facilitates the hypertrophic remodeling of vascular smooth muscle cells (11). Hyperhomocysteinemia is known to be an independent risk factor for ischemic heart disease and stroke, as well as atherosclerosis (12).

At normal levels, Homocysteine has no negative effect on the body. It is only when Homocysteine levels rise above 15  $\mu\text{mol/L}$  that an issue arises. Blood Homocysteine levels can rise above 100  $\mu\text{mol/L}$ , a condition known as severe hyperhomocysteinemia (HHcy), through an enzyme mutation that occurs in one in every hundred thousand live births (13). The mutation is one of N5, N10-methylenetetrahydrofolate reductase (MTHFR). Because 5,10-MTHF is catalyzed into folate, the molecule utilized in the remethylation

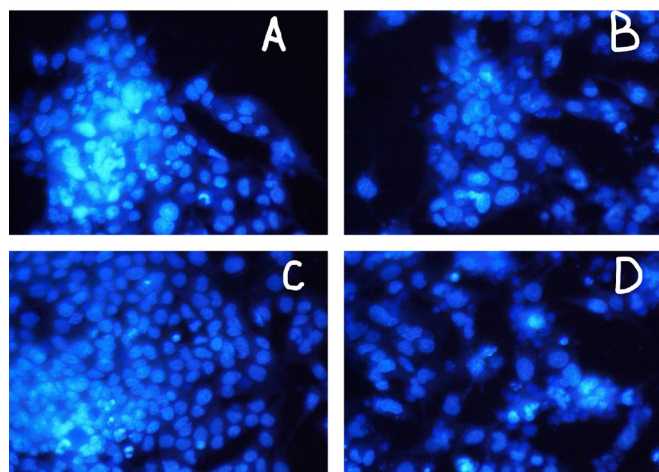


**Figure 1: Fluorescent images of each experimental group.** Images are labelled according to the experimental group they represent. A represents the control, B represents the CXCL1/KC treatment group, C represents the Homocysteine treatment group, and D represents the Homocysteine + CXCL1/KC treatment group.

Trial	Control	CXCL1/ KC	Homo- cysteine	Homocysteine + CXCL1/KC
1	61.026	25.050	70.743	22.417
2	51.239	28.075	83.737	34.603
3	51.405	25.834	57.788	21.080
4	60.407	78.769	59.814	64.667
5	83.286	37.371	72.112	54.715
6	46.118	65.960	71.297	71.042
7	31.782	71.657	75.772	58.015
8	54.112	31.083	44.638	48.793
9	60.833	12.364	78.481	66.866
10	68.061	72.980	56.727	45.231
11	35.415	58.318	66.875	44.417
12	33.843	59.745	79.869	49.003
13	63.731	72.205	61.655	63.750
14	65.789	38.264	55.946	82.382
15	75.546	49.854	75.979	77.667
16	83.205	56.899	67.429	22.417
17	53.577	74.396	79.639	34.603
18	61.026	51.544	48.515	21.080
19	74.146	63.758	82.348	64.667
20	84.175	25.834	52.859	54.715

**Table 1: Average field fluorescence (AU) by trial.** This table displays the average field fluorescence values for each trial obtained using ImageJ.

of Homocysteine, the mutation is a clear cause of hyperhomocysteinemia. A mutation of MTHFR is the most common inborn error of folate metabolism. It is also the most common genetic cause of hyperhomocysteinemia because it prevents the reduction of Homocysteine levels, leading to its accumulation in the heart (13).

HL-1 cells can be serially passaged, yet they maintain the ability to contract and retain differentiated cardiac morphological, biochemical, and electrophysiological properties (14). For these reasons, HL-1 cardiomyocytes will be the test model for the following experiment. A classical immune response would involve the recruitment of T- and B-cells to the site of inflammation by sentinel cells (1). However, due to the lack of these immune cells in the culture, a classical immune response will not be produced. Therefore, this study will focus on the direct effect of CXCL1/KC on cardiomyocytes. Homocysteine will be used as a model for the direct effect of an inflammatory agent on cardiomyocytes. It is expected that cells treated with CXCL1/KC will maintain the cell density of untreated cells; if cells were treated with Homocysteine or both Homocysteine and CXCL1/KC, then they will have a cell density that was higher than that of untreated cells.

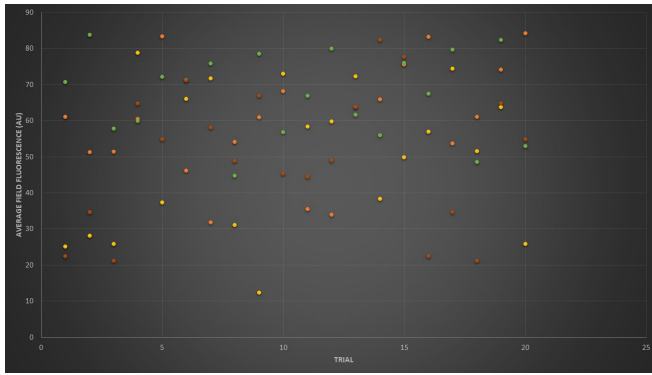


**Figure 2: Average field fluorescence (AU) by trial.** This scatterplot displays the data acquired through recording the mean fluorescence value as measured by Image J for each image taken by a fluorescent microscope following treatment. Orange represents the control, yellow represents the CXCL1/KC treatment, green represents the Homocysteine treatment, and brown represents the Homocysteine + CXCL1/KC treatment.

## RESULTS

The question of whether CXCL1/KC treatment negatively affects cardiomyocytes, signified by a decrease in cell density, was tested by measuring cell density of HL-1 cardiomyocytes treated with CXCL1/KC, Homocysteine, both in combination, or neither. The cells were visualized with DAPI, a blue nuclear stain, yielding a representation of cell density based upon presence of DAPI in the view window. Each field of view revealed cells with their nuclei as blue circular objects and the absence of cells as complete darkness (**Figure 1**). The average field fluorescence value, a relative measure of cell density, was recorded for twenty fields of view for the experimental groups with CXCL1/KC, Homocysteine, both, and neither which had ranges of average field fluorescence values of 12.364-78.769, 44.638-83.737, 21.080-82.382, and 31.782-84.175, respectively (**Table 1**).

The data collected varied greatly within each group due to the nonspecific method of measuring cell density. Viewed individually, the data points appear loosely correlated and the ranges for each group overlap (**Figure 2**). Furthermore, the standard deviations for the experimental groups with CXCL1/KC, Homocysteine, both, or neither are large at 20.409, 11.651, 19.186, 15.772 (**Table 2**). Still, when the values are

Group	Sum	Mean	Variance	Std Dev
Control	1198.72	59.936	248.76	15.772
CX	999.96	49.998	416.52	20.409
Hcy	1342.22	67.111	138.08	11.651
Hcy+CX	1002.13	50.107	368.10	19.186

**Table 2: Summary of Statistics.** This table shows the mean of the average field fluorescence values (AU) for each experimental group (N=20 for all groups), the sum of all values for each group, the mean average field fluorescence per group, variance, and standard deviation. This information summarizes the general statistics about the data collected. Ctrl=Control, CX=CXCL1/KC, Hcy=Homocysteine, and Hcy+CX=Homocysteine + CXCL1/KC.

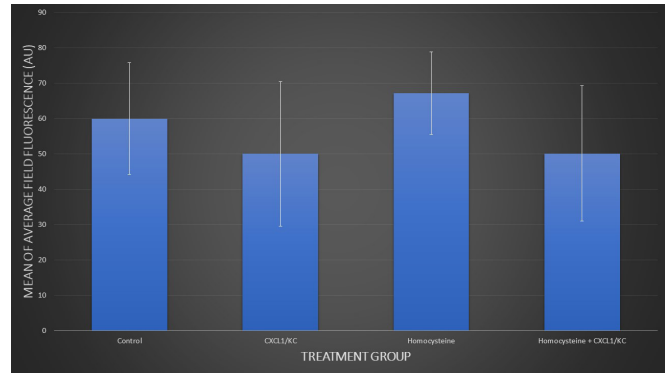


**Figure 3: Mean average field fluorescence (AU) of each treatment group.** This bar graph concisely displays what the effects of each treatment were on average field fluorescence by displaying the mean of each treatment group. The bars are representative of the standard deviation for each group.

averaged, distinct trends can be identified between the test groups. An order of mean average field fluorescence can be established from least to greatest as CXCL1/KC, CXCL1/KC + Homocysteine, Control, and then Homocysteine with means of 49.998, 50.107, 59.936, and 67.111, respectively (**Table 2**, **Figure 3**). The decrease in average field fluorescence (and thus cell density) in both the CXCL1/KC treatment group and the CXCL1/KC + Homocysteine treatment group compared to the control suggests that cardiomyocyte growth and survival is impeded by cytokine treatment. Additionally, the increase in average field fluorescence in the Homocysteine treatment group compared to the control suggests that cell density had increased. This likely occurred as a result of the non-classical immune response provoked by the administration of Homocysteine.

Each group had a high standard deviation: 20.409, 11.651, 19.186, and 15.772 for CXCL1/KC, Homocysteine, both, and neither, respectively, and some overlap between standard deviation bars (**Table 2**, **Figure 3**). Additionally, one-way ANOVA analysis confirmed that there were significant differences between the groups ( $F_{3,76}=4.72$ ,  $P=0.0045$ ) (**Table 3**). Tukey HSD revealed that the significant differences existed between the CXCL1/KC group and the Homocysteine group, as well as the Homocysteine + CXCL1/KC and the Homocysteine group, for a Q critical value of 3.74 (**Table 4**). Although there were no significant differences between experimental treatments and the control, the differences amongst experimental groups can be extended to imply differences between an experimental group and the control group. Although the CXCL1/KC treated cells were expected not to differ from the control group, they had a significantly lower cell density compared to the Homocysteine group. From these results, we can discern that CXCL1/KC did influence cell density. Additionally, the CXCL1/KC + Homocysteine treatment group also had a significantly lower cell density compared to the Homocysteine group. This strengthens the finding that Homocysteine increased cell density and CXCL1/KC decreased it, even when CXCL1/KC was administered

with Homocysteine.

## DISCUSSION

We initially hypothesized that if cells were treated with CXCL1/KC, then cell density would not differ from that of untreated cells. On the other hand, if cells were treated with Homocysteine or both Homocysteine and CXCL1/KC, we predicted that they would have a cell density that was higher than that of the untreated cells. We expected that CXCL1/KC would not alter the cell density because it was expected to only affect inflammation (not modelled here). We expected that Homocysteine would increase cell density because it has been shown to induce inflammation and thus cell proliferation. We also expected that combining Homocysteine with CXCL1/KC would have the same effect as Homocysteine alone because CXCL1/KC was predicted to have no effect.

The first part of our hypothesis, that cells treated with CXCL1/KC will maintain the cell density of untreated cells, was not supported because cell density in CXCL1/KC treated group was significantly decreased compared to the Homocysteine treated group. Given that the control group's average cell density was between the two, it implies that cell density decreased in the CXCL1/KC group and increased in the Homocysteine group compared to the control to create the significant difference between the CXCL1/KC and Homocysteine groups. The second part of our hypothesis, that if cells were treated with Homocysteine or both Homocysteine and CXCL1/KC, then they will have a cell density that was higher than that of untreated cells, was rejected because although treatment with Homocysteine alone resulted in a significant increase when compared to the CXCL1/KC group, the CXCL1/KC + Homocysteine group experienced a significant decrease in cell density when compared to the Homocysteine group.

The cytokine appears to have significantly decreased cell density both by itself and when administered to cells with Homocysteine treatment. Although the Homocysteine group only had a trending increase when compared to the control, this increase was compared to the other two experimental groups. The control itself was an intermediate between the two ends of the cell density spectrum. Both groups that had CXCL1/KC experienced a relative decrease in cell density, which may have been the result of slowed cell proliferation.

The direct effect of CXCL1/KC seems to be beneficial, as it would counteract the cell proliferation associated with the inflammatory response to Homocysteine. Yet, it is concerning that even though Homocysteine treatment increased cell density alone, cell density was decreased overall with the combination treatment. If this result is not attributable to increased cell stress resulting from the application of two treatments, then it may signify that CXCL1/KC directly reduces cell density of cardiomyocytes.

Minor errors may have occurred due to the nature of the measuring instruments used. When using a micropipette to take up small volumes of 15 µl of treatment, we may have taken up slightly more or less volume due to the adhesion of the solution to the end of the pipette tip. Furthermore, when capturing images of the stained cell samples, the movement of the slide required repeated refocusing of the microscope. Due to an inability to refocus to the exact same level each time, although it was nearly the same each time, certain images may have been a little more focused than others, potentially having a small impact on the fluorescence readings.

CXCL1/KC may be a promising treatment for myocarditis. CXCL1/KC has previously been shown to successfully reduce cardiac inflammation, and this experiment revealed that the treatment of myocarditis with CXCL1/KC directly reduces cell proliferation. The treatment reduced cell density of the cardiomyocytes, which would be favorable in the context of reducing inflammation but may be detrimental at the level observed in this study. In the future, researchers could investigate the issue of inflammation induced by Homocysteine and the possibility of reducing this inflammation with CXCL1/

Source of Variation	SS	df	MS	Std Dev
Between	4144.49	3	1381.5	15.772
Within	22257.7	76	292.86	20.409
Total	26402.8	79		11.651
F	4.71719			
F crit	2.724944		p-value	0.004506

**Table 3: ANOVA Test Results.** This table shows the data from the ANOVA one-way statistical test including degrees of freedom and the F critical value.

Comparison	Abs. Difference	Std Error	Q stat	Null hypothesis	Q critical
Ctrl-CX	9.9381	3.827	2.597	Accept	3.74
Ctrl-Hcy	7.1751	3.827	1.875	Accept	
Ctrl-(Hcy+CX)	9.8296	3.827	2.569	Accept	df
CX-Hcy	17.113	3.827	4.472	Reject	60
CX-(Hcy+CX)	0.1085	3.827	0.0283	Accept	
Hcy-(Hcy+CX)	17.005	3.827	4.444	Reject	

**Table 4: Tukey HSD Results.** This table shows the data from the Tukey HSD test and reveals that significant differences exist between the Homocysteine group and both the CXCL1/KC group and the Homocysteine + CXCL1/KC group. Ctrl=Control, CX=CXCL1/KC, Hcy=Homocysteine, and Hcy+CX=Homocysteine + CXCL1/KC.

KC in a more complex model than a simple cell culture. With either mouse tissue or a mouse heart in culture, a study could evaluate the classical immune response to Homocysteine and get a more comprehensive view of the effects of each treatment. Beyond this, a study could focus on the relationship between cardiomyocyte density and heart function since past research has shown that myocarditis reduces heart function. This would bridge the gap between the speculative results of the reduction of cell density seen in our study and more definitive conclusions regarding whether heart function is affected to determine if CXCL1/KC would be effective for reducing inflammation without negative consequences. Such a study would ensure that CXCL1/KC does not worsen heart function or confirm that it does have the detrimental effects suggested by this study.

### MATERIALS AND METHODS

The HL-1 Cardiomyocytes were first cultured in T25 flasks (NEST) with the Claycomb's medium (Sigma Aldrich). The protocols found on the product data sheet were followed to supplement the medium with Fetal Bovine Serum, L-Glutamine, and Penicillin-Streptomycin. After several T25 flasks of HL-1 cardiomyocytes had reached confluency, the number of cells in each flask was determined using a hemocytometer (Thermo Fisher). Half a million cells were transferred into each chamber of a four-chambered cell culture slide (Pipette.com) with 500 microliters of Claycomb's medium.

The cells were left to grow in a 37° Celsius incubator with 5% CO<sub>2</sub> and attach to the slide for three days in which most cells experienced attachment. Afterwards, each treatment was administered to its respective experimental group. The control group received no treatment. The CXCL1/KC group received CXCL1/KC (R&D Systems) solution, dissolved in 1X PBS, to make a 100 nanomolar concentration of CXCL1/KC in the medium. We determined this concentration was appropriate after consultation with other researchers that had experience working with CXCL1/KC. The Homocysteine group received DL-Homocysteine (Sigma Aldrich), dissolved in 1X PBS, to make a 100 micromolar concentration of DL-Homocysteine in the medium. This is a physiologically relevant concentration according to research done at the University of Nebraska (15). Finally, the CXCL1/KC + Homocysteine group received CXCL1/KC and Homocysteine dissolved in PBS to make a solution with the medium of 100 nanomolar CXCL1/KC and 100 micromolar DL-Homocysteine.

After 24 hours, all media was aspirated from the chambers and the cells were fixed using a 4% formaldehyde solution (Sigma Aldrich). Ten minutes later, formaldehyde was aspirated from each chamber and the cells were washed twice with ice cold 1X PBS. Then cells were permeabilized for 10 minutes using 0.01% Triton X-100 solution (Sigma Aldrich). Finally, the cells were incubated with a 1 microgram/milliliter concentration of DAPI (Biolegend) in 1X PBS for 15 minutes at 37 degrees Celsius and in darkness. After incubation, the

DAPI solution was aspirated and any remnant DAPI was removed by 3 washes with 0.1% Tween 20 solution (Sigma Aldrich) in 1X PBS (PBST).

Before putting the slide under the fluorescent microscope, 100 microliters of 1X PBS were added to each chamber to prevent the samples from drying out. The slide was then placed on the stage of the fluorescent microscope in a dark room with the fluorescent violet light on. The cell imaging monitor (EVOS) was then used to visualize and capture images of each chamber. Ten images were taken of each chamber by moving to another area of the chamber and refocusing after each capture. The process was repeated twice to yield 20 images for each experimental group.

The images were analyzed using ImageJ software through Fiji (16). They were individually uploaded to the program and the mean feature of ImageJ was used to determine the average fluorescence of the field of view, referred to as average field fluorescence in this study. This value was used as a relative measure of cell density for the purposes of this research. Statistical analysis was performed by one-way ANOVA and Tukey HSD. A Q critical value of 3.74 was used for 60 degrees of freedom and a p-value of 0.05.

### ACKNOWLEDGEMENTS

This research was done using cardiomyocytes donated by Tetyana Pedchenko of the Vanderbilt Department of Medicine.

Special thanks to Kepa Oyarbide for his assistance with cell culture during this research.

**Received:** April 14, 2018

**Accepted:** June 27, 2018

**Published:** April 26, 2019

### REFERENCES

1. Anft, Michael. "Understanding Inflammation." John Hopkins Health Review, vol. 3, no. 1, 2016, www.johnshopkinshealthreview.com/issues/spring-summer-2016/articles/understanding-inflammation.
2. Shultz, Jason C., et al. "Diagnosis and Treatment of Viral Myocarditis." *Diagnosis and Treatment of Viral Myocarditis*, vol. 84, no. 11, 2009, pp. 1001-09, doi:10.4065/84.11.1001.
3. Cooper, Leslie T., Jr, et al. "The Global Burden of Myocarditis: Part 1: A Systematic Literature Review for the Global Burden of Diseases, Injuries, and Risk Factors." *Global Heart*, vol. 9, no. 1, 2014, pp. 121-29, doi: 10.1016/j.ghart.2014.01.007.
4. Pinto, Yigal M., et al. "Proposal for a Revised Definition of Dilated Cardiomyopathy, Hypokinetic Non-dilated Cardiomyopathy, and Its Implications for Clinical Practice: A Position Statement of the ESC Working Group on Myocardial and Pericardial Diseases." *European Heart Journal*, vol. 37, no. 23, 2016, pp. 1850-58, doi:10.1093/eurheartj/ehv727.
5. Escher, Felicitas, et al. "Myocarditis and Inflammatory



- Cardiomyopathy: From Diagnosis to Treatment." *Turk Kardiyol Dern Ars*, vol. 43, no. 8, 2015, pp. 739-48, doi:10.5543/TKDA.2015.47750.
6. Sagar, Sandeep, et al. "Myocarditis." *Lancet*, vol. 379, no. 9817, 2012, pp. 738-47, doi:10.1016/S0140-6736(11)60648-X.
  7. Bachmaier, Kurt, et al. "Therapeutic Administration of the Chemokine CXCL1/KC Abrogates Autoimmune Inflammatory Heart Disease." *PLoS One*, vol. 9, no. 6, Feb. 2014, doi:10.1371/0100-608.
  8. Carreño, Juan Eduardo, et al. "Cardiac Hypertrophy: Cellular and Molecular Events." *Revista Española De Cardiología*, vol. 59, no. 5, May 2006, doi:10.1016/S1885-5857(06)60796-2.
  9. Shenoy, Vijetha, et al. "Correlation of Serum Homocysteine Levels with the Severity of Coronary Artery Disease." *Indian Journal of Clinical Biochemistry*, vol. 29, no. 3, Aug. 2013, pp. 339-44, doi:10.1007/s12291-013-0373-5.
  10. Byon, Chang Hyun, et al. "Redox Signaling in Cardiovascular Pathophysiology: A Focus on Hydrogen Peroxide and Vascular Smooth Muscle Cells." *Redox Biology*, vol. 9, 2016, pp. 244-53, doi.org/10.1016/j.redox.2016.08.015.
  11. Staiculescu, Marius C., et al. "The Role of Reactive Oxygen Species in Microvascular Remodeling." *International Journal of Molecular Sciences*, vol. 15, no. 12, 2014, pp. 23792-835, doi:10.3390/ijms151223792.
  12. Saluba, Himmatrao, et al. "Homocysteine: Often Neglected but Common Culprit of Coronary Heart Diseases." *Journal of Cardiovascular Disease Research*, vol. 5, no. 3, July 2014, doi:10.11.1.674.2323.
  13. Faeh, D., et al. "Homocysteine as a Risk Factor for Cardiovascular Disease: Should We (still) Worry About?" *Swiss Medical Weekly*, vol. 136, nos. 47-48, Dec. 2006, pp. 745-56, www.ncbi.nlm.nih.gov/pubmed/17225194.
  14. Claycomb, William C., et al. "HL-1 Cells: A Cardiac Muscle Cell Line That Contracts and Retains Phenotypic Characteristics of the Adult Cardiomyocyte." *Proc National Academy of Science USA*, vol. 95, no. 6, Mar. 1998, pp. 2979-84, www.ncbi.nlm.nih.gov/pubmed/9501201.
  15. Kesharwani, Varun, et al. "Hydrogen Sulfide Mitigates Homocysteine-mediated Pathological Remodeling by Inducing MiR-133a in Cardiomyocytes." *Mol Cell Biochem*, vol. 404, nos. 1-2, Mar. 2015, pp. 241-50, doi:10.1007/s11010-015-2383-5.
  16. Schindelin, Johannes, et al. "Fiji: An Open-source Platform for Biological-image Analysis." *Fiji: An Open-source Platform for Biological-image Analysis*, vol. 9, 28 June 2012, pp. 676-82. *Nature*, doi:10.1038/nmeth.2019.

# Sponsorship



Editor's Circle

\$10,000+



Patron

\$5,000+



PORTFOLIOS  
WITH PURPOSE®

## Institutional Supporters



HARVARD  
UNIVERSITY



HARVARD  
MEDICAL SCHOOL



Tufts  
UNIVERSITY

## Charitable Contributions

We need your help to provide mentorship to young scientists everywhere.

JEI is supported by an entirely volunteer staff, and over 90% of our funds go towards providing educational experiences for students. Our costs include manuscript management fees, web hosting, creation of STEM education resources for teachers, and local outreach programs at our affiliate universities. We provide these services to students and teachers entirely free of any cost, and rely on generous benefactors to support our programs.

A donation of \$30 will sponsor one student's scientific mentorship, peer review and publication, a six month scientific experience that in one student's words, 're-energized my curiosity towards science', and 'gave me confidence that I could take an idea I had and turn it into something that I could put out into the world'. **If you would like to donate to JEI, please visit <https://emerginginvestigators.org/support>, or contact us at [questions@emerginginvestigators.org](mailto:questions@emerginginvestigators.org).** Thank you for supporting the next generation of scientists!

'Journal of Emerging Investigators, Inc. is a Section 501(c)(3) public charity organization (EIN: 45-2206379). Your donation to JEI is tax-deductible.'



[emerginginvestigators.org](http://emerginginvestigators.org)